

# Global System for Atmospheric Modeling: Model Description and Preliminary Results

Marat Khairoutdinov<sup>1</sup>, Peter N. Blossey<sup>2</sup>, and Christopher S. Bretherton<sup>2</sup>

<sup>1</sup>Stony Brook University

<sup>2</sup>University of Washington

November 24, 2022

## Abstract

The extension of a cloud-resolving model, the System for Atmospheric Modeling (SAM), to global domains is described. The resulting global model, gSAM, is formulated on a latitude-longitude grid. It uses an anelastic dynamical core with a single reference profile (as in SAM), but its governing equations differ somewhat from other anelastic models. For quasi-hydrostatic flows, they are isomorphic to the primitive equations in pressure coordinates, but with the globally uniform reference pressure playing the role of actual pressure. As a result, gSAM can exactly maintain steady zonally symmetric baroclinic flows that have been specified in pressure coordinates, produces accurate simulations when initialized or nudged with global reanalyses, and has a natural energy conservation equation, despite the drawbacks of using the anelastic system to model global scales. gSAM employs a novel treatment of topography using a type of immersed boundary method, the Quasi-Solid Body Method (QSBM), where the instantaneous flow velocity is forced to stagnate in grid cells inside prescribed terrain. The results of several standard tests designed to evaluate accuracy of global models with and without topography as well as results from real-Earth simulations are presented.

**Global System for Atmospheric Modeling:  
Model Description and Preliminary Results**

Marat F. Khairoutdinov<sup>1\*</sup>, Peter N. Blossey<sup>2</sup>, Christopher S. Bretherton<sup>23</sup>

<sup>1</sup>School of Marine and Atmospheric Sciences and Institute for Advanced Computational Science,  
Stony Brook University, Stony Brook, NY, U.S.A.

<sup>2</sup>Dept. of Atmospheric Sciences, University of Washington, Seattle, WA, USA

<sup>3</sup>Allen Institute for Artificial Intelligence, Seattle, WA

Submitted to

*Journal of Advances in Modeling Earth Systems*

---

\* Corresponding author: Marat Khairoutdinov, marat.khairoutdinov@stonybrook.edu

1     **Abstract**

2             The extension of a cloud-resolving model, the System for Atmospheric Modeling (SAM), to global  
3 domains is described. The resulting global model, gSAM, is formulated on a latitude-longitude grid. It  
4 uses an anelastic dynamical core with a single reference profile (as in SAM), but its governing equations  
5 differ somewhat from other anelastic models. For quasi-hydrostatic flows, they are isomorphic to the  
6 primitive equations in pressure coordinates, but with the globally uniform reference pressure playing the  
7 role of actual pressure. As a result, gSAM can exactly maintain steady zonally symmetric baroclinic flows  
8 that have been specified in pressure coordinates, produces accurate simulations when initialized or nudged  
9 with global reanalyses, and has a natural energy conservation equation, despite the drawbacks of using  
10 the anelastic system to model global scales. gSAM employs a novel treatment of topography using a type  
11 of immersed boundary method, the Quasi-Solid Body Method (QSBM), where the instantaneous flow  
12 velocity is forced to stagnate in grid cells inside prescribed terrain. The results of several standard tests  
13 designed to evaluate accuracy of global models with and without topography as well as results from real-  
14 Earth simulations are presented.

15  
16     **Plain Language Summary**

17             The System for Atmospheric Modeling (SAM), a model widely used to study evolution of clouds  
18 and small-scale atmospheric motions using computational grids with horizontal spacings of several meters  
19 to a few hundred kilometers, has been extended to simulations of the whole Earth with global grid spacings  
20 of 1-5 km that realistically represent intense and localized rain and snow storms. The resulting global  
21 atmosphere model, gSAM, is unique in its use of a computationally efficient approximation to the exact  
22 equations of air motion and its method of representing flow over mountains, which is well suited to steeply  
23 sloped terrain. The paper documents gSAM's updated equations, representation of physical processes,  
24 and computational methods. Despite its algorithmic simplicity, gSAM produces realistic global weather  
25 forecasts and cloud distributions and agrees well with other more complicated global models on standard  
26 benchmarking tests.

27  
28  
29  
30  
31

32 **Key Points**

33

- 34 • The anelastic System for Atmospheric Modeling (SAM) is extended to a global latitude-longitude  
35 grid.
- 36 • The model uses a novel treatment of topography forcing the flow to instantaneously stagnate in  
37 the cells inside prescribed terrain.
- 38 • The model performs well in several standard tests that evaluate the accuracy of global models  
39 and in real-Earth simulations.

40

41 **1. Introduction**

42

43 Global climate change has become one of the most pressing issues of our time and threatens the  
44 way of life and even lives themselves of billions of people. Global climate models (GCMs) have been at  
45 the forefront of the effort to predict the extent of the future climate change as documented in a steady  
46 stream of the IPCC reports (e.g., IPCC 2013; 2021). Although there has been a fair amount of progress on  
47 this long and arduous path to the truth, models with parameterized convection have struggled to represent  
48 the fundamental feedbacks of the climate system to anthropogenic forcing, particularly the feedbacks  
49 associated with clouds (e.g, Randall et al 2003; Stevens and Bony 2013).

50 One way to further advance our understanding of how the climate system responds to the external  
51 influences is to continuously push against the limits of the currently available computer technology by  
52 widening the range of resolved scales of atmospheric motion and improving the realism with which  
53 physical processes are represented. Even though innovative models that test the limits of present-day  
54 computational resources may not be practical for the long simulations required for climate prediction, they  
55 may provide us with clues what is wrong with the current generation of the GCMs, and perhaps, even help  
56 to improve them. One such innovative models that appeared impractical at first but eventually led to  
57 staggering progress in the field of computer modeling of the Earth’s general circulation is NICAM (Tomita  
58 and Satoh 2004). By using a globe-spanning grid with a spacing of less than 5 kilometers, NICAM was  
59 able to explicitly simulate deep convection, thereby becoming the first global storm-resolving model  
60 (GSRM). NICAM was so far ahead of its time that several years passed before other models of similar  
61 class started to appear. Today, more than a dozen global non-hydrostatic models with 2-5 km grid  
62 resolution can run for at least several months at a time.

63           The development of one such GSRM, the global System for Atmospheric Modeling (further  
64 gSAM) was motivated by near-global simulations with its predecessor, the original SAM (Khairoutdinov  
65 and Randall 2003; further SAM), which is a conventional cloud-resolving model on a Cartesian grid.  
66 Those near-global simulations were used to better understand the physics of tropical deep convection and  
67 its interactions with the equatorially trapped waves (Bretherton and Khairoutdinov 2015; Narenpitak et al  
68 2020), the Madden-Julian Oscillation (Khairoutdinov and Emanuel 2018), and tropical cyclogenesis  
69 (Narenpitak et al 2020) within the idealization of an aquaplanet. In those simulations, SAM was applied  
70 to tropical convection over very large domains, which are comparably wide as the actual circumference  
71 of the Earth. The domain was limited in the latitudinal direction by placing solid walls at about 45° latitude,  
72 as further extension using a Cartesian grid would distort the spherical geometry. The walls significantly  
73 distort the nearby atmospheric structure and may affect the simulated Hadley circulation throughout the  
74 domain.

75           Conceptually, it is straightforward to make SAM a truly global model by replacing its Cartesian  
76 grid with a grid based on the spherical coordinates and including simple treatments of terrain and land  
77 surface processes. A major technical obstacle was the solver for the global elliptic equation for pressure.  
78 SAM uses a fast Fourier transform in both horizontal directions, which works only for Cartesian grids  
79 with constant horizontal grid spacing. With colleagues at the Institute for Advanced Computational  
80 Science at Stony Brook University, an efficient hybrid FFT-Geometric Multigrid Solver (FFT-GMG),  
81 based on Lu (2016), has been implemented in gSAM to address this issue. The terrain is treated using a  
82 simple, novel immersed boundary method, unlike in other current GSRMs, which typically use terrain-  
83 following coordinates.

84           The first version of gSAM was completed just in time for DYAMOND (DYnamics of the  
85 Atmospheric general circulation On Non-hydrostatic Domains; Stevens et al 2019), the first GSRM  
86 intercomparison project. DYAMOND was based on a 40-day free run of each GSRM initialized from  
87 reanalysis for 1 Aug. 2016 with specified sea-surface temperatures. The gSAM simulation was quite  
88 competitive with other GSRMs (Satoh et al 2019; Stevens et al 2019), even though little time was available  
89 for model refinement or debugging before the production run. The gSAM is unique among the  
90 DYAMOND GSRMs in the formulation of its dynamical core and terrain, and in being developed  
91 independent of a major modeling center. It is designed to be an easy-to-use extension of SAM, which  
92 itself has a broad user community of cloud-resolving and large eddy simulation modelers.

93 The purpose of this paper is to formally document gSAM and to report the results of several  
 94 standard tests of the global dry dynamical core as well as real Earth simulations. The paper is organized  
 95 as follows. Section 2 describes the model equations, finite-difference approximation, physics packages,  
 96 implementation of terrain, and numerical methods. Results of several tests of the dry dynamical core and  
 97 real Earth simulations are presented in Section 3, followed by conclusions in Section 4.

## 101 2. Model equations and methods

### 103 2.1 Dynamical core

104  
 105 In gSAM, the Cartesian model equations of SAM are reformulated for latitude-longitude  
 106 coordinates on a sphere by redefining the horizontal metric coordinates  $x$  and  $y$  as  $x = r\lambda$  and  $y = r\varphi$ ,  
 107 where  $\lambda$  is longitude,  $\varphi$  latitude, and  $r$  the Earth's radius. The vertical coordinate is height  $z$ . The  
 108 prognostic anelastic conservation equations for the zonal ( $u$ ), meridional ( $v$ ), and vertical ( $w$ ) wind  
 109 components, and for mass are:

$$110 \quad \frac{\partial u}{\partial t} + \frac{1}{\mu} \frac{\partial}{\partial x} uu + \frac{1}{\mu} \frac{\partial}{\partial y} \mu v u + \frac{1}{\bar{\rho}} \frac{\partial}{\partial z} \bar{\rho} w u = -\frac{1}{\mu} \frac{\partial \Phi}{\partial x} + \left( f + \frac{u}{r} \tan \varphi \right) v - f^* w + F_u \quad (1)$$

$$\frac{\partial v}{\partial t} + \frac{1}{\mu} \frac{\partial}{\partial x} uv + \frac{1}{\mu} \frac{\partial}{\partial y} \mu v v + \frac{1}{\bar{\rho}} \frac{\partial}{\partial z} \bar{\rho} w v = -\frac{\partial \Phi}{\partial y} - \left( f + \frac{u}{r} \tan \varphi \right) u + F_v \quad (2)$$

$$\frac{\partial w}{\partial t} + \frac{1}{\mu} \frac{\partial}{\partial x} uw + \frac{1}{\mu} \frac{\partial}{\partial y} \mu v w + \frac{1}{\bar{\rho}} \frac{\partial}{\partial z} \bar{\rho} w w = -\frac{\partial \Phi}{\partial z} + B + f^* u + F_w \quad (3)$$

$$\frac{1}{\mu} \frac{\partial}{\partial x} u + \frac{1}{\mu} \frac{\partial}{\partial y} \mu v + \frac{1}{\bar{\rho}} \frac{\partial}{\partial z} \bar{\rho} w = 0 \quad (4)$$

111  
 112 where  $\mu = \cos \varphi$ ,  $f = 2\Omega \sin \varphi$ ,  $f^* = 2\Omega \cos \varphi$ ,  $\Omega$  is the Earth's angular velocity of rotation,  $\bar{\rho}(z)$  is the  
 113 prescribed reference density profile, which depends on height only,  $\Phi = p'/\bar{\rho}$ , where  $p'$  is the  
 114 perturbation of pressure from the reference profile, buoyancy acceleration  $B = g\alpha'/\bar{\alpha}$ , where  $g$  is  
 115 gravitational acceleration and  $\alpha'$  is the perturbation of specific volume (inverse density) at the reference  
 116 pressure from its reference profile  $\bar{\alpha}(z)$ ,  $F_u, F_v, F_w$  are accelerations due the subgrid-scale (SGS) eddy  
 117 viscosity. The pressure-gradient terms in equations (1)-(3) generally follow the kinetic-energy-conserving

118 version of the anelastic approximation of Lipps and Hemler (1982). The prognostic equation for an  
 119 arbitrary advected scalar  $s$  is given by

$$\frac{\partial s}{\partial t} + \frac{1}{\mu} \frac{\partial}{\partial x} us + \frac{1}{\mu} \frac{\partial}{\partial y} \mu vs + \frac{1}{\bar{\rho}} \frac{\partial}{\partial z} \bar{\rho} ws = S_s + F_s \quad (5)$$

120

121 where  $S_s$  denotes local sources and sinks, and  $F_s$  the divergence of SGS fluxes of  $s$ .

122

## 123 *2.2 Buoyancy and conservation of energy*

124

125 For an anelastic model without moist processes, the thermodynamic equation is naturally  
 126 formulated as prognosis of the potential temperature  $\theta$ . However, for accurate simulation of moist and  
 127 radiative processes, the absolute temperature  $T$  must also be known (e. g. for calculating the saturation  
 128 vapor pressure of water). Over regional domains, the reference pressure profile is a good approximation  
 129 for the pressure field over the entire domain, so the absolute temperature can be estimated from potential  
 130 temperature using the reference pressure profile (Lipps and Hemler, 1992). However, over a global  
 131 domain, the local pressure can differ from the reference pressure at the same height by as much as 10%,  
 132 especially in the middle and upper troposphere. For a given potential temperature, this could change the  
 133 implied absolute temperature by as much as 10 K, which is far too inaccurate for calculating moist  
 134 thermodynamics.

135 Thus gSAM uses a different approach, following Pauluis (2008), who replaced conservation of  
 136 potential temperature by conservation of frozen moist static energy  $h_f = c_p T + gz + L_c q_v - L_f q_{ice}$  (the  
 137 sum of moist enthalpy and geopotential energy), where  $c_p$  is the specific heat of air,  $L_c$ ,  $L_s$  and  $L_f = L_s -$   
 138  $L_c$  are the latent heats of vaporization, sublimation, and freezing,  $q_v$  is water vapor mixing ratio, and  $q_{ice}$   
 139 is the frozen water mixing ratio. This approximation can be consistently derived from the conservation of  
 140 moist entropy by replacing the total pressure with the reference pressure and justified by the scaling  
 141 assumptions used to derive the anelastic approximation. In this same spirit, where pressure is required in  
 142 a moist thermodynamic formula in addition to temperature, gSAM uses the reference pressure rather than  
 143 the full pressure. While pressure perturbations are neglected in moist thermodynamics here, their impact  
 144 was explored in an anelastic framework by Kurowski et al (2013).

145 In a height-coordinate model like gSAM, the conservation equation for frozen moist static energy  
 146 involves tendencies of  $T$  and  $q$ , natural choices for accurately formulating moist thermodynamics, rather

147 than  $\theta$ . Like SAM, gSAM is formulated in terms of a liquid/ice water static energy  $h_L =$   
 148  $h_f - L_c(q_v + q_{liq} + q_{ice}) = c_p T + gz - L_c q_{liq} - L_s q_{ice}$ , where  $q_{liq}$  is the total liquid water mixing  
 149 ratio. Like frozen moist static energy,  $h_L$  is conserved in nearly hydrostatic air motions even with  
 150 reversible phase transitions between water vapor, liquid and ice, but it separates off the water contribution  
 151 to  $h_f$ , which is treated in a separate conservation equation. The prognostic equation for  $h_L$  is a special case  
 152 of equation (5) with the source term:

$$S_{h_L} = -\frac{1}{\bar{\rho}} \frac{\partial}{\partial z} (-L_c P_{liq} - L_s P_{ice}) - wB + c_p Q_{rad} \quad (6)$$

153  
 154 Here  $P_{liq}$  and  $P_{ice}$  are total sedimentation fluxes for liquid and frozen water;  $Q_{rad}$  is the radiative heating  
 155 rate. The buoyancy itself is expressed using absolute temperature as

$$B = g\alpha' / \bar{\alpha} = g((T - \bar{T}) / \bar{T} + 0.608q_v - q_{liq} - q_{ice}) \quad (7)$$

157 An improvement of gSAM over SAM is the inclusion of the effect of the buoyancy flux  $wB$  in (6). As  
 158 emphasized by Pauluis (2008), it is important to include this term for conservation of total energy, as it  
 159 opposes the generation/sink of the vertical kinetic energy by the buoyancy. Note that use of temperature,  
 160 rather than potential temperature, in  $B$  differs from the Lipps-Hemler anelastic equations by neglecting  
 161 the contribution of pressure perturbations to potential temperature perturbations. It is consistent with  
 162 approximating the total pressure with the reference pressure in the dynamical equations, which requires  
 163 that buoyancy contributions due to relative horizontal Exner function perturbations  $(R/c_p)(p'/\bar{p})$  be much  
 164 less than those due to relative horizontal temperature perturbations  $T'/\bar{T}$ . On a global scale, this  
 165 approximation holds well near the surface but less well in the upper atmosphere; nevertheless, we will see  
 166 that it does not substantially degrade the accuracy of gSAM in comparison to models that use fully  
 167 compressible formulations of the flow equations.

168 The total energy is defined as  $E = K + gz + h_f$ , that is the sum of kinetic energy  $K$  and  
 169 thermodynamic energy. Similar to Pauluis (2008), it can be shown that the governing equations of gSAM  
 170 conserve total energy in the whole domain:

$$\frac{\partial}{\partial t} \iiint \bar{\rho} E \mu \, dx \, dy \, dz = SHF + LHF - L_f P_{sf} + R_{NET} \quad (8)$$

171 that is, globally-integrated total energy can only be changed by the total surface flux of frozen moist  
 172 enthalpy  $SHF + LHF - (L_s - L_c)P_{sf}$  and net radiative flux convergence in the atmosphere  $R_{NET}$  (=

173  $R_{SFC} - R_{TOA}$ ), where  $SHF$ ,  $LHF$ , and  $P_{sf}$  are the surface total sensible, latent and frozen precipitation  
 174 fluxes, respectively;  $R_{TOA}$  and  $R_{SFC}$  are the top-of-atmosphere and surface net radiative fluxes.

175

### 176 *2.3 Consistency with primitive equations in pressure coordinates*

177

178 For quasi-hydrostatic flows (when horizontal scale of motions is much larger than the vertical),  
 179 the system of anelastic equations (1)-(4) with thermodynamic equation (6) and buoyancy in form (7) is  
 180 isomorphic to the system of primitive equations used by many GCMs. Assuming that the reference state  
 181 is in hydrostatic balance, that is  $d\bar{p} = -g\bar{\rho}dz$ , defining pressure vertical velocity  $\omega = -g\bar{\rho}w$ , using the  
 182 dry expression for buoyancy based on equation (7), neglecting terms with  $f^*$ , and neglecting the vertical  
 183 acceleration, the dry system of equations (1)-(4) and (7) can be rewritten, using the horizontal Cartesian  
 184 coordinates for clarity, as

$$\frac{\partial u}{\partial t} + u \frac{\partial u}{\partial x} + v \frac{\partial u}{\partial y} + \omega \frac{\partial u}{\partial \bar{p}} = -\frac{\partial \Phi}{\partial x} + fv \quad (9)$$

$$\frac{\partial v}{\partial t} + u \frac{\partial v}{\partial x} + v \frac{\partial v}{\partial y} + \omega \frac{\partial v}{\partial \bar{p}} = -\frac{\partial \Phi}{\partial y} - fu \quad (10)$$

$$0 = -\frac{\partial(\Phi + gz)}{\partial \bar{p}} - \frac{RT}{\bar{p}} \quad (11)$$

$$\frac{\partial u}{\partial x} + \frac{\partial v}{\partial y} + \frac{\partial \omega}{\partial \bar{p}} = 0 \quad (12)$$

$$\frac{\partial T}{\partial t} + u \frac{\partial T}{\partial x} + v \frac{\partial T}{\partial y} + \omega \left( \frac{\partial T}{\partial \bar{p}} + \frac{RT}{c_p \bar{p}} \right) = 0 \quad (13)$$

185

186 which is an exact form of the primitive equations (PE) in pressure coordinates based on the reference  
 187 pressure profile. Note that it is important for the derivation of the system (9)-(13) to have the buoyancy in  
 188 the form (7) and to include the buoyancy flux term as a source of  $h_L$  in equation (6).

189

The isomorphism of our anelastic system in the hydrostatic limit with the primitive equations  
 190 can be an advantage both for dynamical reasoning and for initialization from or nudging to a global  
 191 reanalysis. For instance, the equations of geostrophic balance are the same in both systems (although the  
 192 interpretation of  $\Phi$  is slightly different), and thermal wind balance can be expressed very similarly by  
 193 replacing  $p$  by  $\bar{p}$  for gSAM, that is, for PE:

194

$$f \frac{\partial u}{\partial p} = -\frac{\partial}{\partial p} \frac{\partial \Phi}{\partial y} = \frac{R}{p} \frac{\partial T}{\partial y}$$

195 while in gSAM:

$$196 \quad f \frac{\partial u}{\partial \bar{p}} = - \frac{\partial}{\partial \bar{p}} \frac{\partial \Phi}{\partial y} = \frac{R}{\bar{p}} \frac{\partial T}{\partial y}.$$

197 Based on this analogy, a good way to initialize gSAM from reanalysis fields is to interpolate the input  
198 data in pressure coordinates to the anelastic reference pressures  $\bar{p}(z_k)$  corresponding to the model height  
199 levels  $z_k$ . A suitable gSAM reference profile  $\bar{p}(z)$  is constructed by calculating the globally averaged  
200 geopotential height at the reanalysis pressure levels and interpolating this function to obtain the reference  
201 pressures at the known heights  $z_k$ . The reference density is computed from the hydrostatic balance of the  
202 reference pressure profile. This approach will preserve approximate dynamical balances (such as thermal  
203 wind balance) in the reanalysis, where they occur.

204 To illustrate the result of such a procedure, we initialized gSAM with the fields from the ERA5  
205 reanalysis on pressure coordinates at 00Z on January 20, 2020, used for initialization of the most recent  
206 DYAMOND-Winter project ([https://www.esiwace.eu/services/dyamond-initiative/services-dyamond-](https://www.esiwace.eu/services/dyamond-initiative/services-dyamond-winter)  
207 [winter](https://www.esiwace.eu/services/dyamond-initiative/services-dyamond-winter)). We ran gSAM on the same horizontal grid as the ERA5 for one hour to let the fields to adjust to  
208 the topography. Then we used gSAM’s diagnosed  $\Phi = p'/\bar{\rho}$  field to obtain the pressure perturbation of  
209 pressure  $p'$  which is added to the reference pressure profile to obtain the total pressure field. In Figure 1,  
210 the resultant pressure at the surface of the topography is compared to the ERA5 surface pressure. gSAM  
211 reproduces the surface pressure quite well, especially over the ocean. Some biases over land are mostly  
212 explained by differences in the vertical model grid, topography dataset and interpolation techniques. The  
213 difference map clearly shows the imprint of the “staircase” pattern of gSAM surface topography (to be  
214 discussed further below) on its surface pressure.

215

## 216 *2.4 Physics*

217

218 Many physics packages in gSAM are directly inherited from SAM. The formulation of the subgrid-  
219 scale (SGS) fluxes employs two approaches, the 1.5-order closure based on the prognostic SGS turbulent  
220 kinetic energy (TKE) and a simpler Smagorinsky-type closure, used in global simulations, which assumes  
221 perfect balance between shear/buoyancy production of TKE and its viscous dissipation. Several  
222 microphysics modules are available: the original SAM’s single-moment microphysics, and three  
223 comprehensive bulk microphysics modules imported from the Weather Research and Forecasting model  
224 (WRF): the Morrison et al (2005), Thompson et al (2008), and P3 (Morrison and Milbrandt, 2015). There

225 are two choices of radiation. The first is from the Community Atmosphere Model version 3 (CAM3;  
226 Collins et al 2006), and the second is the Rapid Radiative Transfer Model (RRTM; Iacono et al 2008),  
227 from the Community Earth System Model version 1 (Hurrell et al 2013). The former is faster than the  
228 latter, but less accurate.

229 The land surface module is based on the Simplified Land Model (SLM), originally developed for  
230 SAM by Lee and Khairoutdinov (2015). There are 16 land types as defined by the International  
231 Geosphere-Biosphere Program (IGBP) classification system. Each type defined visible and near-infrared  
232 albedos, leaf area index, characteristics of the root system, roughness length and displacement height for  
233 surface flux computations, among others. The output of SLM includes land and ice surface sensible and  
234 latent heat fluxes, surface albedo for visible and near-infrared radiation, surface skin temperature for  
235 longwave radiation, and snow depth. The soil has 9 levels, with thicknesses gradually increasing from 1  
236 cm at the surface to 1 m below. Soil hydraulic and heat conduction properties depend on the clay, sand,  
237 and water contents and change sharply if a soil layer is frozen. In addition to soil, SLM computes heat  
238 fluxes inside glaciers and sea ice, the depth of which is prescribed from observations. Also, there are  
239 parameterizations of accumulation and melting of snow, accumulation of rainwater on tree leaves, surface  
240 runoff and flooding. Planned future publications will provide more details on SLM in gSAM. Over the  
241 ocean, surface flux and albedo parameterizations from CAM3 are used, as in SAM.

242  
243 *2.5 Numerics*

245 The finite-difference approximations for the equations in gSAM are formulated on Arakawa C-  
246 grid, like in SAM, that is, all scalars are defined at the grid-cell centers, while velocity components on  
247 grid-cell's sides. Using coordinate transformations, gSAM's model equations can be written and  
248 discretized in forms analogous to the Cartesian grid forms used by SAM. By simply setting  $\mu = 1$  and  
249  $\tan \varphi = 0$  in all the equations, gSAM can seamlessly be switched from a global storm-resolving model to  
250 a large-eddy simulation (LES) or a cloud-resolving model (CRM) and thereby include all the functionality  
251 of original SAM. gSAM's latitude-longitude grid can also be used for large-area regional modeling where  
252 a Cartesian grid would lead to a substantial loss in accuracy. For such regional modeling, gSAM uses  
253 strong nudging to the prescribed fields at narrow zones along the domain boundaries.

254 The advection scheme for all scalars is the fully 3-D monotonic and positive transport MPDATA  
255 (Smolarkiewicz 2006), as in SAM. Subgrid-scale fluxes and their divergence, as in equation (5), are

256 discretized using conventional centered finite differences. Also following SAM, the momentum equations  
 257 are integrated in time using the explicit third-order Adams-Bashforth (AB3) time scheme. One of the main  
 258 reasons for using the AB3 scheme is the use of the second order centered difference (SOC) scheme in flux  
 259 form for advection of momentum with the property of conservation not only of momentum but also of  
 260 kinetic energy, which also helps to control non-linear instability. The AB3 scheme allows a relatively high  
 261 maximum Courant number of 0.72 with SOC and is slightly dissipative, which helps to damp the two  
 262 computational modes inherent in AB3. A disadvantage of AB3 is its strict numerical instability threshold  
 263 for diffusion  $\Delta t < 0.1 k/\Delta^2$ , where  $k$  is diffusion coefficient, and  $\Delta$  is grid spacing. This may cause a  
 264 serious problem when simulating deep convection and using relatively high vertical resolution in the  
 265 boundary layer, where relatively large SGS eddy-diffusivity coefficients, predicted by the SGS model,  
 266 could affect the model stability. AB3 also has also a rather restrictive stability criterion that in Newtonian  
 267 damping terms, the damping timescale must be longer than about two time-steps (Duran 1991). Therefore,  
 268 in gSAM, we introduced an additional implicit step for vertical diffusion and damping. The workflow  
 269 over each time step goes as follows. First, a provisional solution is found using the AB3 scheme as

$$270 \quad u^* = u^n + \Delta t^n (aA^{n-1} + bA^{n-1} + cA^{n-2}) \quad (14)$$

271 where  $A$  denotes the advection, SGS diffusion (with the exception of the “fast” terms such as the vertical  
 272 diffusion or strong-damping terms), Coriolis, but not the pressure-gradient terms;  $a$ ,  $b$ , and  $c$  are the AB3  
 273 coefficients that depend on current  $\Delta t^n$  and past time steps  $\Delta t^{n-1}$  and  $\Delta t^{n-2}$  (Fiedler and Trapp, 1993).  
 274 Next, a first correction is made to  $u^*$  to include vertical diffusion and damping, denoted here by  $\mathbf{B}$ , using  
 275 the implicit step:

$$276 \quad u^{**} = u^* + \Delta t^n \mathbf{B}(u^{**}) \quad (15)$$

277 Finally, a pressure-correction step is performed to enforce anelastic mass conservation (4):

$$278 \quad u^{n+1} = u^{**} - \Delta t^n (a\nabla\Phi^n + b\nabla\Phi^{n-1} + c\nabla\Phi^{n-2}) \quad (16)$$

279 The unknown scaled perturbation pressure  $\Phi^n$  is diagnosed from the Poisson equation

$$280 \quad \nabla(\rho\nabla\Phi^n) = \frac{1}{a\Delta t^n} \nabla \cdot \rho u^{**} - \frac{b}{a} \nabla(\rho\nabla\Phi^{n-1}) - \frac{c}{a} \nabla(\rho\nabla\Phi^{n-2}) \quad (17)$$

281 The procedure above is identical to the time integration of the momentum equations employed by SAM  
 282 except for the implicit step (15).

283 The Cartesian grid in SAM has constant horizontal grid spacings in  $x$  and  $y$  for which the elliptic  
 284 equation (17) has coefficients that depend only on height; therefore, a bi-directional FFT in the horizontal  
 285 directions is used to obtain a tridiagonal system of equations for the vertical structure of the horizontal

286 Fourier coefficients. An inverse bi-directional FFT of their solutions yields  $\Phi^n$ . This direct method of  
287 solving (17) is non-iterative and can be efficiently parallelized across many computational cores.

288 For the latitude-longitude grid employed by gSAM, the coefficients of equation (17) also depend  
289 on latitude, so the bi-directional FFT method can no longer be applied. However, in the usual case that  
290 the horizontal grid spacing in the longitudinal direction is constant for each latitudinal circle, none of the  
291 coefficients depend on longitude. Then an FFT can still be applied in that direction, yielding a set of  
292 independent two-dimensional (latitude-height) Helmholtz equations for the longitudinal Fourier  
293 coefficients that can be solved in parallel. For gSAM, the height-latitude grid is highly anisotropic, with  
294 thousands of grid cells in the latitudinal direction and only in the order of a hundred in the vertical. In  
295 addition, the vertical grid is generally much finer, at least in the low troposphere, than the horizontal grid.  
296 Attempts to use freely available generic multigrid solvers have failed because of very low convergence  
297 rates for such anisotropic grids with Neuman boundary conditions which would make gSAM too  
298 expensive to be practical. Therefore, a custom geometric multi-grid (GMG) solver for anisotropic 2-D  
299 Helmholtz equations has been developed (Lu 2016). The resultant hybrid FFT-GMG solver is nearly as  
300 efficient as the original bi-directional FFT solver when applied on a grid of similar size. When Cartesian  
301 coordinates are used in gSAM, the conventional non-iterative bi-directional FFT solver is still used.

302 Because of the latitude-longitude grid, the equations have a singularity at the pole. In the early  
303 development version of gSAM that participated in the DYAMOND project, this problem was  
304 circumvented by placing a solid wall around each of the poles at about 89° latitude circle. In the current  
305 version of gSAM, the grid goes all the way to the poles, so that the horizontal face of the cells in the last  
306 row of the grid cells has a triangular shape because the poleward face of otherwise quadrilateral cells  
307 degenerates into a point, so the corresponding fluxes, computed on C-grid, through that face are identically  
308 zero. The other faces of the polar cells don't have the singularity problem. For other terms, such as  
309 Coriolis, when the velocity at the pole is required, the nearest point with valid value of meridional velocity  
310 is used instead. To minimize considerable reduction of the timestep because of potentially high CFL  
311 numbers in the zonal direction right near the pole, the artificial damping of the horizontal velocity is  
312 performed to prevent the CFL from exceeding the critical value. This, of course can distort the solution  
313 right near the poles. This problem will be mitigated in the future by using local grid coarsening for the  
314 advection in zonal direction (e.g., Asaithambi and Mahesh 2017).

315 One of the benefits of not using the FFT transform in the  $y$  direction on latitude-longitude grid is  
316 that the grid spacing in  $y$  can be variable. By varying grid spacing with latitude, the local (in meters, not

317 in degrees) in  $y$  can be the same as resolution in  $x$ , effectively covering most of the Earth with a grid that  
 318 is locally isotropic in the horizontal but has a somewhat broader grid spacing in the tropics than in the  
 319 midlatitudes. In practice, such a grid is used only to about  $70^\circ$  latitude, and further refinements in  $y$  are  
 320 avoided when approaching the poles, for stability reasons. Such an approach provides about twice as high  
 321 resolution in midlatitudes than over the equator using the same number of latitudinal grid circles as would  
 322 be used for a uniformly spaced grid.

323

## 324 2.6 Terrain

325

326 A global model without representation of topography would be of little utility beyond idealized  
 327 aqua-planet studies. Note that SAM has no capability to represent topography. One of the most popular  
 328 methods for incorporating terrain in atmospheric models is to use a terrain following coordinate system.  
 329 However, this would mean abandoning both the bi-directional FFT solver for the Poisson equation (17)  
 330 for pressure in SAM and hybrid FFT-GMG solver in gSAM, replacing them with a fully 3-D multigrid  
 331 solver. Designing such a solver and making its computational and parallel performance as efficient as the  
 332 existing solvers in SAM and gSAM would be a very challenging task. Instead, a variant of a so-called  
 333 body force method has been implemented. In this approach, the velocity of the flow inside a solid obstacle  
 334 is forced to stagnate, similar to using a fictitious Newtonian damping (Chen and Leach, 2007;  
 335 Smolarkiewicz et al, 2007). However, we introduce a novel aspect to that approach. We cannot simply set  
 336 the velocity inside the topography to zero at the end of each time step, as this would violate mass  
 337 conservation (Eqn. 4). Instead, we damp the flow inside an obstacle using the implicit correction step (15),  
 338 used before applying the pressure gradient terms, which would look in the case of Newtonian damping  
 339 with time scale  $\tau$  as

$$340 \quad \mathbf{u}^{**} = \mathbf{u}^* - \mathbf{u}^{**} \frac{\Delta t^n}{\tau} \quad (18)$$

341 Step (18) is computationally stable for any value of  $\tau$ , and can be rewritten as

$$342 \quad \mathbf{u}^{**} = \mathbf{u}^* \frac{1}{1 + \frac{\Delta t^n}{\tau}} \quad (19)$$

343 For instantaneous relaxation  $\tau = 0$ , the factor  $1/(1 + \Delta t^n/\tau)$  becomes also zero, so that the  
 344 damping is equivalent to  $\mathbf{u}^{**} = 0$  inside an obstacle and there is no need to specify a value for  $\tau$ . The

345 modified  $\mathbf{u}^{**}$  is used then in the right-hand-side of the Poisson equation (17), solution of which is used to  
346 compute the final velocity  $\mathbf{u}^{n+1}$  for the current time step.

347 The approach, which we called the Quasi-Solid Body Method (QSBM; Khairoutdinov et al 2022),  
348 has the virtue of simplicity, as it requires very little change to the model code (and no change to the  
349 structure of the Poisson solver), and can, in principle, be adopted by any anelastic model. Moreover, the  
350 method works not only for topography, but also buildings. For that case, the method has already been  
351 tested by comparing the simulated flow around a single rectangular building to the wind-tunnel  
352 observations with good results (Khairoutdinov et al, 2022).

353 There are drawbacks to the QSBM. First, the method does not guarantee that the velocity inside  
354 the terrain remains completely stagnant, as some residual flow is unavoidable. However, the magnitude  
355 of the residual velocities is found to be very small, typically one to two orders of magnitude smaller than  
356 the velocity of the incoming flow, even in the case of a building. The simulation can further be improved  
357 by reapplying the QSBM to the solution at the end of the time step, although each such iteration increases  
358 the expense of the model because of the repeated use of the elliptic equation solver. Khairoutdinov et al  
359 (2021) performed up to three such additional iterations and found that each iteration reduces the residual  
360 velocities inside the building further by about a factor of two. For example, for an oncoming wind of  
361 several meters per second, the maximum residual flow was only several centimeters per second. However,  
362 it was also found that the additional iterations result in only minor simulation improvement compared to  
363 the observations, and therefore, can generally be omitted in most cases.

364 Another drawback of the QSBM is that the topography can be represented only by whole grid  
365 cells, resulting in “staircase”-like mountain shapes and poor representation of gently sloped terrain.  
366 Therefore, the method works the best for buildings and very steep terrain. In the past, several methods  
367 have been developed to address such a problem, for example the “shaved cells” approach (Adcroft et al.  
368 1997). However, such methods would result in an elliptic equation (17) having coefficients that are  
369 functions of longitude as well, which prevent the use of an FFT in zonal direction and would require a  
370 more complex 3-D multigrid solver.

371 “Staircase” terrain can generate short-wave (two-delta) noise around obstacles. In gSAM, a  
372 numerically dissipative third-order upstream-biased scheme (TOB) is used to help to control the small-  
373 scale noise around topography. To minimize overdamping by the TOB scheme, the hybrid scheme is  
374 employed to compute the momentum advection tendency a weighted superposition of the momentum  
375 tendencies due to SOC and TOB schemes. The TOB scheme used together with the AB3 is somewhat less

376 stable than the SOC scheme, with a maximum stable Courant number of about 0.39 vs 0.72. However, the  
377 stability threshold of the hybrid scheme changes almost linearly with the weighting coefficient  $\alpha$  between  
378 the stability thresholds of the SOC and TOB schemes. Experimentally, using a 1-D advection test, the  
379 following empirical relationship between maximum stable Courant number (CFL) and partitioning weight  
380  $\alpha$  is found:  $CFL = 0.39 + 0.23\alpha + 0.09\alpha^2$ . For example, for  $\alpha=0.7$ , that is 70% of momentum tendency  
381 due to SOC and 30% due to TOB scheme, which is usually sufficient to control the short-wave noise, the  
382 maximum stable Courant number is about 0.6, compared to 0.72 if only SOC is used. This reduces the  
383 maximum time step required to maintain a stable solution by about 20%.

384

### 385 **3. Results**

386

#### 387 *3.1 Steady state test (gradient-wind balance)*

388

389 To demonstrate that gSAM's anelastic approach indeed gives results equivalent to the primitive  
390 equations in pressure coordinates in the hydrostatic limit, as discussed above in Section 2.4, the idealized  
391 steady-state case developed by Jablonowski and Williamson (JW06; 2006) is used. The initial conditions  
392 in JW06 describe a steady-state rotating atmosphere in the hydrostatic and gradient-wind balance as an  
393 analytic solution to the primitive equations. The prescribed structure of the zonally symmetric temperature  
394 distribution and corresponding zonal thermal wind are shown in Figs. 2a-b and closely resembles the real  
395 atmosphere. A perfect model based on the primitive equations should maintain that initial gradient-wind  
396 balance indefinitely without developing any instabilities or meridional circulation. For the test, we use a  
397 relatively coarse 512x256 horizontal grid (approximately  $0.7^\circ$  uniform grid spacing) with 30 vertical levels  
398 whose spacing gradually reduces from about 100 m near the surface to 5000 m near the domain top at 37  
399 km. This is comparable to the GCM grids used in the JW06 study. The time step is 30 s. As suggested by  
400 JW06, no explicit noise damping or SGS diffusion is applied. The non-dissipative SOC scheme is used  
401 for advection of momentum. To minimize round-off errors, all computations are done in double precision.  
402 Following the discussion in Section 2.3, the specified initial temperature and velocity fields are not  
403 interpolated from pressure-sigma to height coordinates; instead, they are interpolated to the reference  
404 pressures corresponding to the gSAM height levels, calculated following Sec. 2.3 with the global-mean  
405 geopotential height as a function of pressure calculated by integrating the hydrostatic equation vertically  
406 with the globally averaged temperature profile and surface pressure prescribed by JW06. This approach

407 enables gSAM to preserve the initial thermal wind balance of the unperturbed basic state specified in  
408 pressure coordinates.

409

410 Starting from the prescribed zonal velocity and temperature fields, the model is integrated for 30  
411 days. The resultant zonal wind remains nearly steady, developing slight wind anomalies with the  
412 amplitudes of less than about 0.1 m/s even in the region of jets in midlatitudes, as shown for day 30 in  
413 Fig. 2c. Note that the reference pressure profile is used as the vertical coordinates on these plots. Even  
414 smaller errors are found for the meridional wind (not shown). The slight imbalance can be explained by  
415 the relatively coarse grid used in this test. As expected, the gSAM initialization procedure and numerics  
416 almost precisely maintain the thermal wind balance of the prescribed temperature field and zonal wind,  
417 even though they were designed for pressure/sigma-coordinate models. The corresponding geopotential  
418 height proxy  $\Phi/g + z$  computed by gSAM, shown in Fig. 3d, is nearly identical to the geopotential height  
419 prescribed in JW06 (see their Fig. 1e).

420

### 421 3.2 Baroclinic wave test

422

423 The zonally symmetric state in the previous test is baroclinically unstable, and baroclinic waves  
424 can be triggered from a relatively small-amplitude initial zonal wind perturbation in mid-latitudes as  
425 described in JW06. The model is run for 10 days with such an initial perturbation and the same grid as  
426 described in the previous test. Snapshots of the surface pressure and of the temperature and vorticity at  
427 850 hPa are shown in Fig. 3. As there is no analytical solution, we compared our results to numerous  
428 results from other dynamical cores found in literature, including JW06. Overall, the magnitudes and the  
429 shapes of the displayed fields compare quite well with other dynamical cores, with the notable exception  
430 of the longitudes of the disturbances, which seem to be advanced forward by about  $10^\circ$  in gSAM. A similar  
431 result was reported by Kurowski et al (2015), who directly compared results from compressible and  
432 anelastic versions of the same model, although for a somewhat different moist baroclinic wave test. They  
433 attributed that advance to the delayed onset of the rapid growth of the baroclinic wave in their anelastic  
434 version of the model. In our case, the initial conditions may also play a role in the apparent phase bias of  
435 the baroclinic wave, as the initial wind perturbation specified by JW06 does not satisfy the anelastic  
436 continuity equation. As the result, gSAM immediately tries to make the flow non-divergent, reducing the

437 amplitude of the initial zonal wind perturbation from 1 m/s to 0.5 m/s, and also creating a rather strong  
438 perturbation of the meridional wind, which is initially absent.

439

### 440 3.3 *Held-Suarez test*

441

442 Held and Suarez (1994; further HS94) developed a standard test of how well dry dynamical cores  
443 simulate statistical properties of mid-latitude baroclinic eddies. The test prescribes highly idealized  
444 diabatic heating and cooling as well as the boundary layer damping. The model then runs for very long  
445 time to obtain the time-averaged statistics. As there is no analytical solution or observations, the model  
446 results are typically compared to the results of other dynamical cores. We run gSAM for 1200 days using  
447 a 288x144x30 grid (uniform 1.25° spacing in latitude and longitude) with the domain top at 37 km and a  
448 20 s time step. The Smagorinsky closure is used for the SGS fluxes, with SOC differences of momentum  
449 fluxes. Above 22 km, a sponge layer is used to control vertically propagating gravity waves. The initial  
450 state is motionless isothermal atmosphere with the temperature of 300K.

451 After allowing 200 days for model spin-up, statistics are calculated over the last 1000 days and  
452 shown in Fig. 4. Overall, the results agree well, both qualitatively and quantitatively, with the climatology  
453 in HS94 as well as other models. For example, Figure 4 compares the zonal wind, meridional eddy-flux  
454 of zonal momentum and meridional eddy flux of temperature to the results obtained by CAM with a  
455 spectral Eulerian dynamical core (CAM-EUL) running with T85 truncation and 30 levels, comparable in  
456 resolution to the grid used by gSAM in this test. The plots for CAM were obtained from its official website  
457 <https://www.cesm.ucar.edu/models/simpler-models/held-suarez.html>. One can see that, in general, gSAM  
458 and CAM-EUL agree quite well in the position, structure and strength of the westerlies in midlatitudes  
459 and of the easterlies in the tropics and polar regions, as well the meridional eddy fluxes of momentum and  
460 heat. The zonally averaged temperature also looks quite similar to HS94 results. A kinetic energy spectrum  
461 for midlatitudes shows the canonical  $k^{-3}$  power law for the large-scale eddies transitions to a  $k^{-5/3}$  power  
462 law for relatively short scales, which is consistent with the observed spectra in the real atmosphere in mid-  
463 latitudes (e. g. Nastrom and Gage, 1985).

464

### 465 3.4 *3-D Rossby-Haurwitz wave*

466

467 This test is an extension of a standard 2-D test for the shallow water models discussed by  
468 Williamson et al (1992). We use the formulation of the 3-D test as described by Jablonowski et al (2008).  
469 Despite being formally a 3-D test, the wave itself is essentially a 2-D barotropic wave, propagating  
470 westward with a constant speed and preserving its shape. Therefore, it is a very useful test to check the  
471 implementation of the Coriolis and metric terms and the ability of the model to maintain such a wave for  
472 long time. The domain has 576x288x30 grid points (0.625° horizontal grid spacing and 30 levels), and  
473 time step is set to 30 s. The number of wavelengths around the equator is set to 4, which corresponds to a  
474 propagation speed of about -15.2° per day, or 24 days for the full revolution around the globe, which is  
475 the model's integration time in this case. Figure 4 shows zonal and meridional wind components as well  
476 as the surface pressure at the end of the run. The propagation speed computed from the Hovmöller diagram  
477 (not shown) turned out to be very close to this theoretical value. The shape and magnitude of the simulated  
478 fields in Fig 4 are barely different from the initial fields after 24 days of integration.

479

### 480 3.5 *Non-hydrostatic mountain waves*

481

482 The tests presented thus far have dealt with quasi-hydrostatic large-scale flows. The present test  
483 examines the non-hydrostatic response of gSAM to flow over the terrain profile proposed in Schär et al  
484 (2002; further S02), which prescribes a series of bell-shaped mountains with the tops inside a cosine-like  
485 envelope. Two cases are considered, a 2-D mountain range case following S02, who also provided an  
486 analytical solution, and a 3-D circular mountain following the case 2.1 from the DCMIP 2012 (Ullrich et  
487 al 2012), for which linear analytical solution has also been developed (Klemp et al 2015; further K15).  
488 For this test we use gSAM in Cartesian coordinates as our goal here is primarily to test the implementation  
489 of the terrain. The atmosphere is isothermal at 300 K, with uniform wind of 20 m/s. The domain has  
490 512x512x80 grid points with 333.3 m grid spacing to make the domain similar in size to the domain in  
491 S02, with the top at 37 km. The vertical grid spacing gradually increases with height, from 40 m near the  
492 surface, to 500 m at 3600 m, staying constant up to 19 km, and then again monotonically increasing to  
493 1400 m at 37 km. The maximum height of the terrain is 250 m with 5000 m mountain-range half-width  
494 and 4000 m mountain wavelength, which represents the distance between individual mountain peaks. This  
495 vertical grid is the same one used by gSAM in DYAMOND (Stevens et al, 2019) and was not specially  
496 refined for this specific test. As the result, the terrain is represented rather coarsely in the vertical by only  
497 6 grid levels below the highest mountain peak. To avoid reflection of gravity waves from the top of the

498 domain, a sponge layer is placed above 20 km. Vertical cross-sections of vertical velocity after two hours  
499 of simulation are shown in Figs. 6a and 6b for the 2-D and 3-D cases, respectively. Both simulations agree  
500 quite well with the analytical solutions Figs. 6c and 6d, which are adopted from K15. There is little  
501 evidence of the effect of terrain “staircasing” on the simulation, mostly because of the use of hybrid SOC-  
502 TOB momentum advection in the vicinity of the mountain with  $\alpha=0.7$  (see sec. 2.6 for details). There are  
503 some additional perturbations compared to the linear analytical solution, probably because of nonlinear  
504 effects. Horizontal cross-sections of vertical velocity for 3-D simulation at 8 and 16 km are shown in Figs.  
505 7a and 7b. They also compare quite well to the analytical solutions Figs. 7c and 7d, also adopted from  
506 K15.

507

### 508 *3.6 Mountain induced Rossby wave train*

509

510 This is another test of the terrain implementation in gSAM, this time for hydrostatic flow over the  
511 globe. The case set-up follows the specifications in the DCMIP 2008 report (Jablonowski et al, 2008).  
512 The base state is an isothermal atmosphere in zonally symmetric solid-body rotation, which is constant  
513 with height, with maximum wind at the equator of 20 m/s. This base state is perturbed by an idealized  
514 bell-shaped 2000-m high mountain, with half-width of 1500 km, centered at 90°E and 30°N. The grid  
515 configuration is similar to the Rossby-Haurwitz wave case. To minimize reflection of gravity waves from  
516 the model top, a sponge layer in the upper third of the domain is employed. The solution for the zonal and  
517 meridional wind components at 700 mb levels at days 5, 15 and 25 are shown in Fig. 8. There is no  
518 analytical solution for this case, but the results compare well with those from other models shown in  
519 DCMIP report by Jablonowski (2008; Fig. 20) and also by Ullrich and Jablonowski (2012). As noted by  
520 the latter, the models in this test usually begin to diverge after 15 simulated days.

521

### 522 *3.7 DYAMOND-Winter real Earth simulation*

523

524 So far, we presented the results of several idealized tests, just a few of many that have been  
525 developed over the years. Such idealized tests have been routinely used by the weather and climate  
526 modelling communities to identify the problems with models’ formulation, their major weaknesses, and  
527 for finding “bugs” in their code that would be difficult to find otherwise in realistic simulations, as many  
528 of the problems and bugs could be simply hidden in the general clatter and noise of such simulations.

529 However, gSAM is not a new model per se: it is an extension of the well-established SAM to a global  
530 domain. Aside from the topography implementation, the rest of the physics in gSAM is basically identical  
531 to SAM's. Therefore, in addition to the tests of the dry dynamical core, cloud-resolving simulations of the  
532 real Earth have been also performed and evaluated. Because of the considerable computational cost of  
533 such realistic simulations, relatively few of them have been performed to date. The very first such  
534 simulation was for the aforementioned DYAMOND project (Stevens et al, 2019), for which the results of  
535 gSAM have been quite encouraging. The model has also performed short hindcast simulations using  
536 different microphysical schemes during the SOCRATES (Southern Ocean Clouds, Radiation, Aerosol  
537 Transport Experimental Study) field experiment, as reported by Atlas et al (2021) whose analysis focused  
538 on a comparison of mixed-phase clouds over the Southern Ocean simulated by different microphysical  
539 parameterizations implemented in SAM. Recently, gSAM has also participated, among several other  
540 GSRMs, in the second phase of the DYAMOND project. Below, we present just a few highlights from  
541 that simulation, reserving more substantial discussion and analysis for future publications.

542 The DYAMOND-Winter simulation covers a 40-day period from January 20<sup>th</sup> to March 1<sup>st</sup>, 2020.  
543 Initialized from ERA5 reanalysis at 00Z on January 20<sup>th</sup>, gSAM ran for 40 days using prescribed sea  
544 surface temperatures and sea ice cover. The CAM3 radiation and standard SAM's single-moment  
545 microphysics are used. The grid has 9216 x 4608 grid cells in the horizontal and 74 levels in the vertical.  
546 The grid spacing is locally isotropic in the horizontal (same in both meridional and zonal directions) until  
547 about 70°N/S with grid spacing of 4.25 km over the equator, gradually decreasing to 2-3 km in  
548 midlatitudes, then coarsening towards the poles to maintain numerical stability. The time step is 10 s.

549 Figure 9 compares the 5-day average (January 21<sup>st</sup> to January 25<sup>th</sup>) of precipitation, surface latent  
550 heat flux (LHF), and top-of-atmosphere (TOA) outgoing longwave (OLR) and absorbed solar (ASR)  
551 radiative fluxes to ERA5 reanalysis. These five days are used to make a quantitative comparison to  
552 reanalysis before the model divergence from the observed state due to natural variability. The first day  
553 has been neglected to allow for model spin-up. Overall, the geographic pattern of the mean precipitation  
554 is reproduced quite well, and gSAM's global mean precipitation of 3.0 mm/day is similar to the 2.9  
555 mm/day five-day average in ERA5. The most notable bias of gSAM is the relatively light precipitation in  
556 the South Pacific Convergence Zone (SPCZ) in tropics. It is encouraging to see orographically enhanced  
557 precipitation zones over the southern tip of South America and the Pacific coast of Colombia, as well as  
558 over Norway, the Pacific Northwest, and South Africa, implying that gSAM's representation of the  
559 topography works reasonably well. The geographic distribution of the surface LHF also compares quite

560 well to ERA5 estimates, with a global mean value of 83.9 W/m<sup>2</sup> in gSAM and 80.0 W/m<sup>2</sup> in ERA5. The  
561 performance of gSAM’s land model is validated by good agreement with ERA5 for LHF over land,  
562 especially over the heavily vegetated areas of tropics and subtropics, where these fluxes vary strongly due  
563 to the diurnal cycle and also depend on partitioning of total flux between the evapotranspiration and  
564 sensible heat fluxes.

565 The simulated pattern of OLR compares well to ERA5, showing large areas filled with cold cloud  
566 tops over tropical land masses, the SPCZ, and major storm-tracks in midlatitudes. In cloud-free areas over  
567 subtropical oceans, the OLR tends to be overestimated, but is underestimated over convectively active  
568 regions over land in tropics. The overall pattern of the ASR is simulated by gSAM reasonably well, but  
569 there are many regional biases, most prominently over the Southern Ocean. Atlas et al (2021) showed that  
570 the low bias in ASR over the Southern Ocean seen in Fig. 9d can be removed by using a microphysics  
571 scheme in gSAM that more efficiently glaciates supercooled shallow cumuli. Global mean OLR is higher  
572 in gSAM than in ERA5, 245.4 W/m<sup>2</sup> vs 240.2 W/m<sup>2</sup>, while at the same time, global mean ASR is  
573 considerably underestimated in gSAM relative to ERA5, 241.6 W/m<sup>2</sup> vs 248.8 W/m<sup>2</sup>. Therefore, the net  
574 incoming radiative flux at TOA (ASR-OLR) is -3.8 W/m<sup>2</sup> in gSAM vs 8.6 W/m<sup>2</sup> in ERA5, a difference  
575 of about 12 W/m<sup>2</sup>. While radiative fluxes from ERA5 should not be considered “ground truth”, this large  
576 discrepancy between gSAM and ERA5 warrants further investigation, including its sensitivity to the  
577 choice of radiation and microphysics packages in gSAM.

578

### 579 *3.8 Hindcast of Hurricane Irma*

580

581 Although weather forecasting was never a motivation for the extension of SAM to a global domain,  
582 the ability of gSAM to forecast a tropical cyclone has been tested by performing a hindcast of Hurricane  
583 Irma, one of the most powerful Atlantic hurricanes of the 2017 season. Irma reached Category 5,  
584 devastated several Caribbean islands, struck Cuba and the Florida Keys, and eventually made landfall in  
585 Florida. Global numerical weather prediction models had difficulty forecasting its path. For example, Fig.  
586 10a shows a so-called “spaghetti” plot with predicted tracks of Irma as of September 5th, 2017 based on  
587 forecasts from several NWP models, approximately 5-6 days before landfall in Florida. One can see a  
588 wide spread of the trajectories with no clear indication on which coast of Florida (east or west) Irma would  
589 make landfall. After initialization from ERA5 reanalysis at 00Z on September 5, gSAM was run for 7  
590 days. After initialization, the sea-surface temperature was not updated since a real forecast model would

591 not have such information. An ensemble of 10 simulations was made with coarse, 17-km grid spacing  
592 using a global 2304x1152 grid, along with one high-resolution deterministic run using 4.25-km spacing  
593 using a 9216 x 4608 grid. All runs used 74 vertical levels and a domain top at 37 km, and no cumulus  
594 parameterization was employed. The ensemble was used to determine the most probable path of Irma,  
595 while the deterministic run was used to make the intensity forecast. All runs were performed on the  
596 Cheyenne supercomputer at NCAR using 1152 cores for the ensemble runs and 4608 cores for the  
597 deterministic run. Each ensemble member ran about 50 times faster than wall-clock time, while the  
598 deterministic simulation ran 6 times faster than wall-clock time. Note that gSAM could run on twice as  
599 many processors as this, which would further increase the throughput by about 80%. For a 7-day forecast,  
600 each of the ensemble runs (which could be done concurrently) would then take less than 2 wall-clock  
601 hours, and the deterministic forecast would take about 16 hours.

602 Figure 10b compares the predicted tracks of Irma from all runs with the estimated best track from  
603 observations. The ensemble generates a wide spread of tracks toward the end of the runs, with the  
604 ensemble mean following the actual path of Irma quite well and correctly predicting that Irma would make  
605 landfall on the east coast of Florida. Fig 10c shows one “lucky” ensemble member that predicted the actual  
606 path of Irma almost perfectly. Figs 10e and 10f show the minimum surface pressure and maximum  
607 sustained wind near the surface as well as best-track data. Because of ERA5’s rather coarse resolution,  
608 the initial depression associated with Irma was relatively weak, so it took several days for the model to  
609 properly spin up the hurricane. As expected, 17-km resolution is not sufficient for predicting the minimum  
610 pressure and intensity of the hurricane but can be useful for predicting its path. The 4-km deterministic  
611 forecast predicts the intensity much better despite not being the best in predicting the hurricane's track.  
612 Overall, the results produced by gSAM in this hurricane case are encouragingly realistic given the  
613 approximations inherent in gSAM’s dynamical equations. This gives a more favorable view of gSAM’s  
614 ability to simulate tropical cyclones than the DYAMOND analysis of Judt et al. (2021) and shows that  
615 gSAM is suitable for both realistic and idealized global simulations requiring storm-resolving grid  
616 resolution.

617  
618  
619  
620  
621

#### 4. Conclusions

This paper describes the extension of the cloud-resolving and large eddy simulation model, SAM, to a global domain. The resulted global storm resolving model, gSAM, is formulated on a latitude-longitude grid but can seamlessly switch back to Cartesian coordinates. Hence, it can still be used as a conventional large-eddy simulation or cloud-resolving model over limited domains. The latitude-longitude grid allows gSAM to run both globally and over very large regional domains for which a Cartesian grid is not sufficiently accurate because of the Earth's curvature.

gSAM is unique among GSRMs in using an anelastic dynamical core with a single reference profile, like past versions of SAM. However, the anelastic equations used in gSAM, which follow Pauluis (2008), differ from most other anelastic models in ways that are helpful for global modeling. Buoyancy in gSAM is based on the absolute temperature, not the potential temperature, and the prognostic thermodynamic equation is based on a moist form of the static energy, rather than potential temperature; these modifications are convenient for microphysical parameterization. The thermodynamic equation also includes the vertical flux of buoyancy (Pauluis, 2008). The resulting system is shown to conserve the global integral of the sum of the kinetic, thermodynamic, and potential energies. For quasi-hydrostatic flows, the anelastic system in gSAM is isomorphic to the primitive equations in pressure coordinates, but with the globally-uniform reference pressure (which is a known function of height) in gSAM playing the role of actual pressure. Therefore, to preserve geophysically important relationships such as geostrophic and hydrostatic balance, initialization of gSAM by external data should be done by mapping horizontal velocity, temperature and other data in pressure coordinates to the reference pressures of each grid level, instead of using a direct column-by-column interpolation of the data to height coordinates. If this is done in a standard gradient-wind balance test, gSAM can exactly maintain steady zonally symmetric baroclinic flows that have been specified in pressure coordinates. This isomorphism helps rationalize how gSAM can simulate realistic global temperature and wind distributions even though assumptions underlying the anelastic approximation, such as the smallness of horizontal pressure perturbations, become shaky on global scales.

Several tests of gSAM's accuracy in simulating global-scale flows without topography were presented. Results of a standard baroclinic-wave test compare quite well to other models' results. In a Held-Suarez test, the mean general circulation agrees well with results from the Community Atmosphere Model with Eulerian dynamical core at similar horizontal grid resolution. In a barotropic equatorial

653 Rossby-Haurwitz wave test, gSAM accurately maintains the expected shape and magnitude of the wave  
654 very well and propagates the wave in the westward direction at a speed very close to the theoretically  
655 derived value.

656 The treatment of topography in gSAM is novel among global atmospheric models, which generally  
657 use terrain-following coordinates. gSAM uses altitude as the vertical coordinate. This considerably  
658 simplifies the discretized fluid transport equations, but it means that some grid points lie within regions  
659 of elevated terrain. The surface boundary condition is enforced using a type of immersed boundary  
660 method, the Quasi-Solid Body Method (QSBM), in which the flow velocity in grid cells inside prescribed  
661 terrain is stagnated using “instantaneous” relaxation to zero. The QSBM method works well, as  
662 demonstrated by two tests: linear non-hydrostatic flow over an idealized mountain range and a global  
663 simulation hydrostatic Rossby waves induced by a large circular mountain. Starting with a no-topography  
664 model version, implementing the QSBM requires minimal code changes and no algorithmic change to the  
665 sophisticated multigrid anelastic Poisson solver used in gSAM.

666 Several results were presented from a real-Earth simulation performed for the DYAMOND-Winter  
667 project. We compared several important fields with ERA-5 reanalysis, such as precipitation, surface latent  
668 heat flux and top-of-atmosphere OLR and solar radiation, averaged over January 21-25, 2020. Despite  
669 several notable biases, the gSAM results track the reanalysis well over this relatively short period.

670 We also presented results of a hindcast of Hurricane Irma in 2017. We used a 17-km grid to  
671 perform a 10-member ensemble runs and high-resolution 4-km for a single deterministic run initialized  
672 from the ERA5 data five days before Irma’s landfall in Florida. The ensemble predicts the hurricane track  
673 quite well but considerably underpredicts the hurricane intensity just before landfall. In contrast, the  
674 deterministic run predicts an intensity similar to that observed, both in minimum surface pressure and  
675 maximum surface wind.

676 Our future research with gSAM will be conducted on multiple fronts. We will continue working  
677 on improving the accuracy of simulations around the poles and on achieving optimal computational  
678 performance on evolving high-performance computing architectures. We plan to run gSAM in weather-  
679 nudged mode, forced by reanalysis data, with different microphysical packages, to improve representation  
680 of clouds and radiation and better understand how different cloud microphysics parameterizations affect  
681 the results. We will evaluate the simulation of the diurnal cycle over land, especially of precipitation, and  
682 work on further improvement of the Simplified Land Model and especially its treatment of snow cover.

683 We will further evaluate the suitability of gSAM (including regional versions that can be used with finer  
684 grids) for forecasting extreme weather events in present and future climates.

685

686 **Acknowledgements** We thank Prof. Xiangmin Jiao, and his students Cao Lu and Oliver Yang from the Dept. of  
687 Applied Mathematics and Statistics and the Institute for Advanced Computational Science at Stony Brook  
688 University for their help in developing and implementing an efficient GMG pressure solver in gSAM. Marat  
689 Khairoutdinov was supported by the NSF grant AGS-1418309 to Stony Brook University and by subaward to  
690 NSF grant AGS-1660604 to University of Washington. Chris Bretherton and Peter Blossey were supported by  
691 NSF grants AGS-1660604 and OISE- 1743753. We would like to acknowledge high-performance computing  
692 support from Cheyenne (doi:10.5065/D6RX99HX) provided by NCAR's Computational and Information  
693 Systems Laboratory, sponsored by the NSF. The data from dynamical core tests is accessible through NCAR  
694 Campaign Storage via Globus. The DYAMOND data is archived by the German Climate Computing Centre  
695 (DKRZ) through the ESIWACE project (<https://www.esiwace.eu/services/dyiamond>).

696

697

698

699

700

701

702

703

704

705

706

707

708

709

710

711

712

713

## References

- 714  
715
- 716 Adcroft, A., Hill, C., Marshall, J., 1997: Representation of topography by shaved cells in a height  
717 coordinate ocean model. *Mon. Wea. Rev.* *125*, 2293–2315
- 718 Asaithambi R., and K. Mahesh, 2017: A note on a conservative finite volume approach to address  
719 numerical stiffness in polar meshes. *J. Comp. Phys.*, *341*, 377-385.
- 720 Atlas, R., C. S. Bretherton, M. F. Khairoutdinov, P. N. Blossey, 2021: Hallett-Mossop rime splintering  
721 dims the Southern Ocean: New insight from global cloud-resolving simulations. *AGU Advances*, in  
722 review, doi:10.1002/essoar.10507321.2.
- 723 Bretherton, C.S., and M. Khairoutdinov, 2015: Convective self-aggregation feedbacks in near-global  
724 cloud-resolving simulations of an aquaplanet. *J. Adv. Model. Earth Syst.*, *7*, 1765-1787,  
725 doi:10.1002/2015MS000499
- 726 Chan, S. T., and Leach, M. J., 2007: A validation of FEM3MP with Joint Urban 2003 data. *J. Appl.*  
727 *Meteor. and Clim.*, *12*, 2127–2146.
- 728 Collins, W. D., and Coauthors, 2006: The formulation and atmospheric simulation of the Community  
729 Atmosphere Model version 3 (CAM3). *J. Climate*, *19*, 2144–2161.
- 730 Durran, D. R. (1991). The third-order Adams-Bashforth method: An attractive alternative to leapfrog  
731 time differencing. *Mon. Wea. Rev.*, *119*, 702-720.
- 732 Judt, F. D., and 25 others, 2021: Tropical Cyclones in Global Storm-Resolving Models, *J. Meteor. Soc.*  
733 *Japan*. Ser. II, No. 3, 579-602. [doi:10.2151/jmsj.2021-029](https://doi.org/10.2151/jmsj.2021-029)
- 734 Fiedler, B. H., and R. J. Trapp, 1993: A Fast Dynamic Grid Adaption Scheme for Meteorological Flows.  
735 *Mon. Wea. Rev.*, *121*, 2879-2888.
- 736 Held, I. M., and M. J. Suarez, 1994: A proposal for the intercomparison of the dynamical cores of  
737 atmospheric general circulation models, *Bull. Amer. Meteorol. Soc.*, *75*, 1825–1830.
- 738 Hurrell, J. W.; M. M. Holland; P. R. Gent (2013). "The Community Earth System Model: A Framework  
739 for Collaborative Research". *Bull. Amer. Meteorol. Soc.*, *94*, 1339–1360.
- 740 Iacono, M. J., Delamere, J. S., Mlawer, E. J., Shephard, M. W., Clough, S. A., and Collins, W. D.  
741 (2008), Radiative forcing by long-lived greenhouse gases: Calculations with the AER radiative  
742 transfer models, *J. Geophys. Res.*, *113*, D13103, doi:[10.1029/2008JD009944](https://doi.org/10.1029/2008JD009944).

743 IPCC 2013: Climate Change 2013: The Physical Science Basis. Contribution of Working Group I to the  
744 Fifth Assessment Report of the Intergovernmental Panel on Climate Change. Cambridge University  
745 Press. Retrieved from <https://www.ipcc.ch/report/ar5/wg1/>, doi:10.1017/CBO9781107415324

746 IPCC, 2021: AR6 Climate Change 2021: The Physical Science Basis. <https://www.ipcc.ch/report/ar6/wg1/>

747 Jablonowski C, and D.L. Williamson, 2006. A baroclinic instability test case for atmospheric model  
748 dynamical cores. *Q. J. R. Meteorol. Soc.*, 132, 2943–2975.

749 Jablonowski, C., P.H. Lauritzen, M.A. Taylor, R.D. Nair, 2008: Idealized test cases for the dynamical  
750 cores of atmospheric general circulation models: a proposal for the NCAR ASP 2008 summer  
751 colloquium, Technical Report.  
752 [http://www-personal.umich.edu/~cjablono/NCAR\\_ASP\\_2008\\_idealized\\_testcases\\_29May08.pdf](http://www-personal.umich.edu/~cjablono/NCAR_ASP_2008_idealized_testcases_29May08.pdf)

753 Khairoutdinov, M. F., and D.A. Randall, 2003: Cloud-resolving modeling of the ARM summer 1997  
754 IOP: Model formulation, results, uncertainties and sensitivities. *J. Atmos. Sci.*, 60, 607-625.

755 Khairoutdinov, M., and K. Emanuel, 2018: Intraseasonal variability in a cloud-permitting near-global  
756 equatorial aqua-planet model. *J. Atmos. Sci.*, 75, 4337-4355, doi:10.1175/jas-d-18-0152.1

757 Khairoutdinov, M. F., A. M. Vogelmann, and K. Lamer, 2022: Adding building resolving capabilities  
758 into the System for Atmospheric Modeling using the Quasi-Solid Box Method. *J. Adv. Model. Earth*  
759 *Syst.*, submitted. Preprint: doi:10.1002/essoar.10509425.1

760 Klemp, J. B., W. C. Skamarock, and S.-H. Park, 2015: Idealized global nonhydrostatic atmospheric test  
761 cases on a reduced-radius sphere, *J. Adv. Model. Earth Syst.*, 7, 1155–1177,  
762 doi:10.1002/2015MS000435.

763 Kurowski, M. J., W. W. Grabowski, and P. K. Smolarkiewicz, 2013: Toward multiscale simulation of  
764 moist flows with soundproof equations, *J. Atmos. Sci.*, 70, 3995-4011. [https://doi.org/10.1175/JAS-](https://doi.org/10.1175/JAS-D-13-024.1)  
765 [D-13-024.1](https://doi.org/10.1175/JAS-D-13-024.1)

766 Kurowski, M. J., W.W. Grabowski, and P. K. Smorarkiewicz, 2015: Anelastic and compressible  
767 simulation of moist dynamics at Planetary Scales. *J. Atmos. Sci.*, 72, 3975-3995.

768 Lee, J. K., and M. Khairoutdinov, 2015: Simplified Land Model (SLM) for use in cloud resolving  
769 models: Formulation and evaluation. *J. Adv. Model. Earth Syst.*, 7, doi:10.1002/2014MS000419

770 Lipps, F., and R. Hemler, 1982: A scale analysis of deep moist convection and some related numerical  
771 calculations. *J. Atmos.Sci.*, 39, 2192-2210.

772 Lu, C, 2016: Efficient Iterative and Multigrid Solvers with Applications, Ph.D. Dissertation, Stony  
773 Brook University Thesis and Dissertations Collection, <http://hdl.handle.net/11401/77232>

774 Morrison, H. and J. A. Milbrandt, 2015: Parameterization of Cloud Microphysics Based on the  
775 Prediction of Bulk Ice Particle Properties. Part I: Scheme Description and Idealized Tests, *J. Atmos.*  
776 *Sci.*, 72, 287–311, <https://doi.org/10.1175/JAS-D-14-0065.1>

777 Morrison, H., J. A. Curry, and V. I. Khvorostyanov, 2005: A new double-moment microphysics  
778 parameterization for application in cloud and climate models. Part I: Description. *J. Atmos.*  
779 *Sci.*, 62, 1665–1677, <https://doi.org/10.1175/JAS3446.1>.

780 Narenpitak, P., C. S. Bretherton, and M. Khairoutdinov, 2017: Cloud and circulation feedbacks in a  
781 near-global aquaplanet cloud-resolving model. *J. Adv. Model. Earth Syst.*, 9, 1069-1090,  
782 doi:10.1002/2016MS000872.

783 Narenpitak P., C. S. Bretherton, and M. F. Khairoutdinov, (2020). The role of multiscale interaction in  
784 tropical cyclogenesis and its predictability in near-global aquaplanet cloud-resolving simulations. *J*  
785 *Atmos Sci.*, 77, 2847-2863

786 Nastrom, G.D., and Gage, K. S., 1985: A climatology of atmospheric wavenumber spectra of wind and  
787 temperature observed by commercial aircraft. *J. Atmos. Sci.*, 42, 950-960.

788 Pauluis O., 2008: Thermodynamic consistency of the anelastic approximation for a moist atmosphere. *J.*  
789 *Atmos. Sci.*, 65, 2719-2729

790 Randall, D., M. Khairoutdinov, A. Arakawa, and W. Grabowski, 2003: Breaking the cloud  
791 parameterization deadlock. *Bull. Amer. Meteorol Soc.*, 84, 1547–1564.

792 Satoh, M., B. Stevens, F. Judt, M. Khairoutdinov, S.-J. Lin, W. Putman, and P. Dueben, 2019: Global  
793 cloud-resolving models, *Curr. Clim. Change Rep.*, <https://doi.org/10.1007/s40641-019-00131-0>

794 Schär, C., D. Leuenberger, O. Fuhrer, D. Lüthi, and C. Girard (2002). A new terrain-following vertical  
795 coordinate formulation for atmospheric prediction models. *Mon. Wea. Rev.* 130, 2459–2480.

796 Smolarkiewicz, P.K., 2006: Multidimensional positive definite advection transport algorithm: an  
797 overview, *Int. J. Numer. Methods Fluids.* 50, 1123–1144.

798 Smolarkiewicz, P. K., Sharman, R., Weil, J., Perry, S. G., Heist, D., & Bowker, G. (2007). Building  
799 resolving large-eddy simulations and comparison with wind tunnel experiments. *Journal of*  
800 *Computational Physics*, 227, 633–653.

801 Stevens B, and S. Bony, 2013: What are climate models missing? *Science*, 340, 1053–1054.

802 Stevens, B., Satoh, M., Auger, L., Biercamp, J., Bretherton, C. S., Chen, X., P. Dueben, F. Judt, M.  
803 Khairoutdinov, D. Klocke, C. Kodama, L. Kornblueh, S.-J. Lin, W. Putman, R. Shibuya, P.  
804 Neumann, N. Roeber, B. Vanniere, P.-L. Vidale, N. Wedi, L. Zhou (2019). DYAMOND: The

805 DYNamics of the Atmospheric general circulation MOdeled on Non-hydrostatic Domains. *J. Meteor.*  
806 *Soc. Japan.*, 6, <https://doi.org/10.1186/s40645-019-0304-z>

807 Thompson, G., P. R. Field, R.M. Rasmussen, and W.D. Hall, 2008: Explicit forecasts of winter  
808 precipitation using an improved bulk microphysics scheme. Part II: Implementation of a new snow  
809 parameterization. *Mon. Wea. Rev.*, 136, 5095–5115, <https://doi.org/10.1175/2008MWR2387.1>.

810 Tomita H, and M. Satoh, 2004: A new dynamical framework of nonhydrostatic global model using the  
811 icosahedral grid. *Fluid Dyn Res.*, 34, 357–400.

812 Ullrich, P. A., C. Jablonowski, J. Kent, P. H. Lauritzen, R. D. Nair, and M. A. Taylor (2012), Dynamical  
813 Core Model Intercomparison Project. (DCMIP) Test Case Document, Earth System CoG.  
814 [[http://www-personal.umich.edu/~cjablono/DCMIP-2012\\_TestCaseDocument\\_v1.7.pdf](http://www-personal.umich.edu/~cjablono/DCMIP-2012_TestCaseDocument_v1.7.pdf)]

815 Ullrich, P. A., and C. Jablonowski, 2012: MCore: A non-hydrostatic atmospheric dynamical core  
816 utilizing high-order finite-volume methods, *J. Comp. Phys*, 231, 5978-5108.

817 Williamson, D.L., J. Drake, J. Hack, R. Jakob, and P. Swarztrauber, 1992: A standard test set for  
818 numerical approximations to the shallow water equations in spherical geometry, *J. Comp. Phys.* 102,  
819 211–224

820

821

822

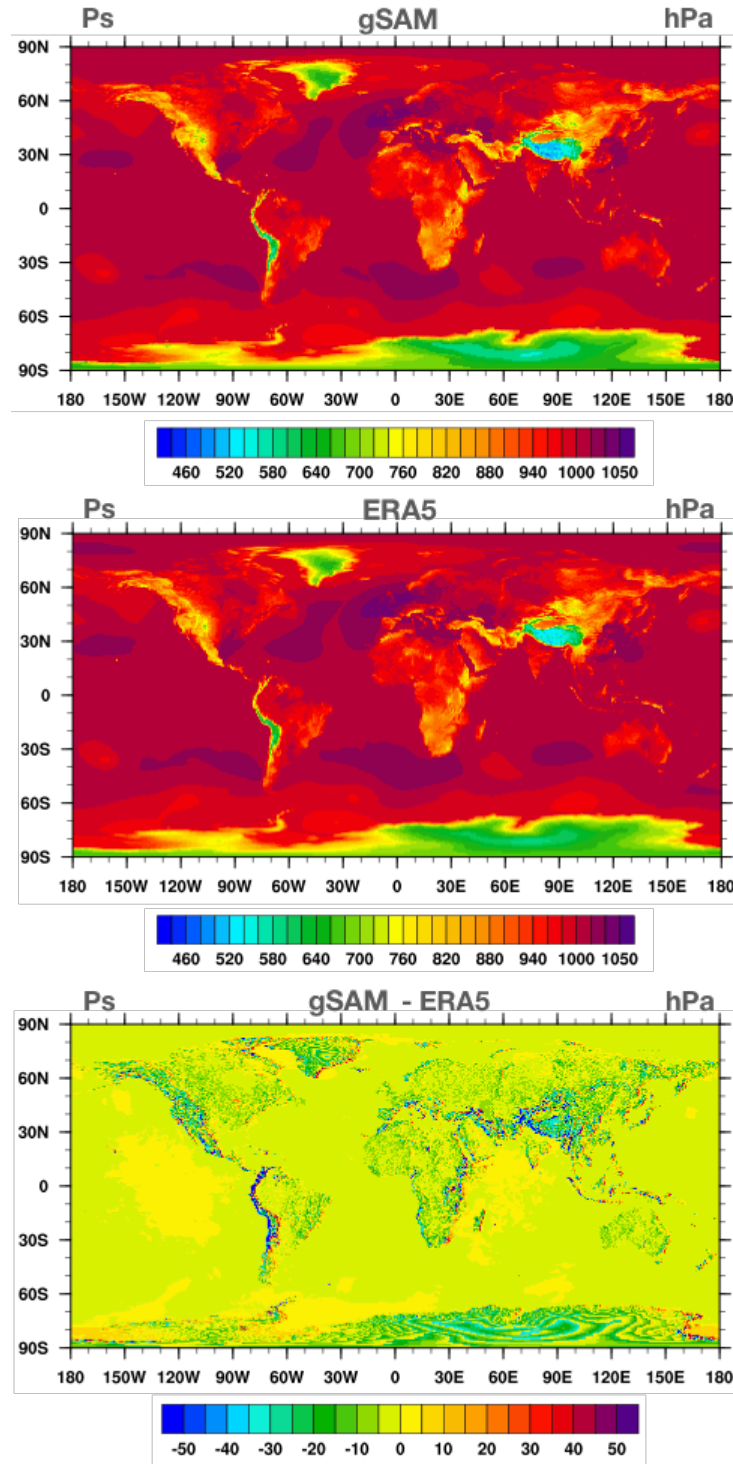
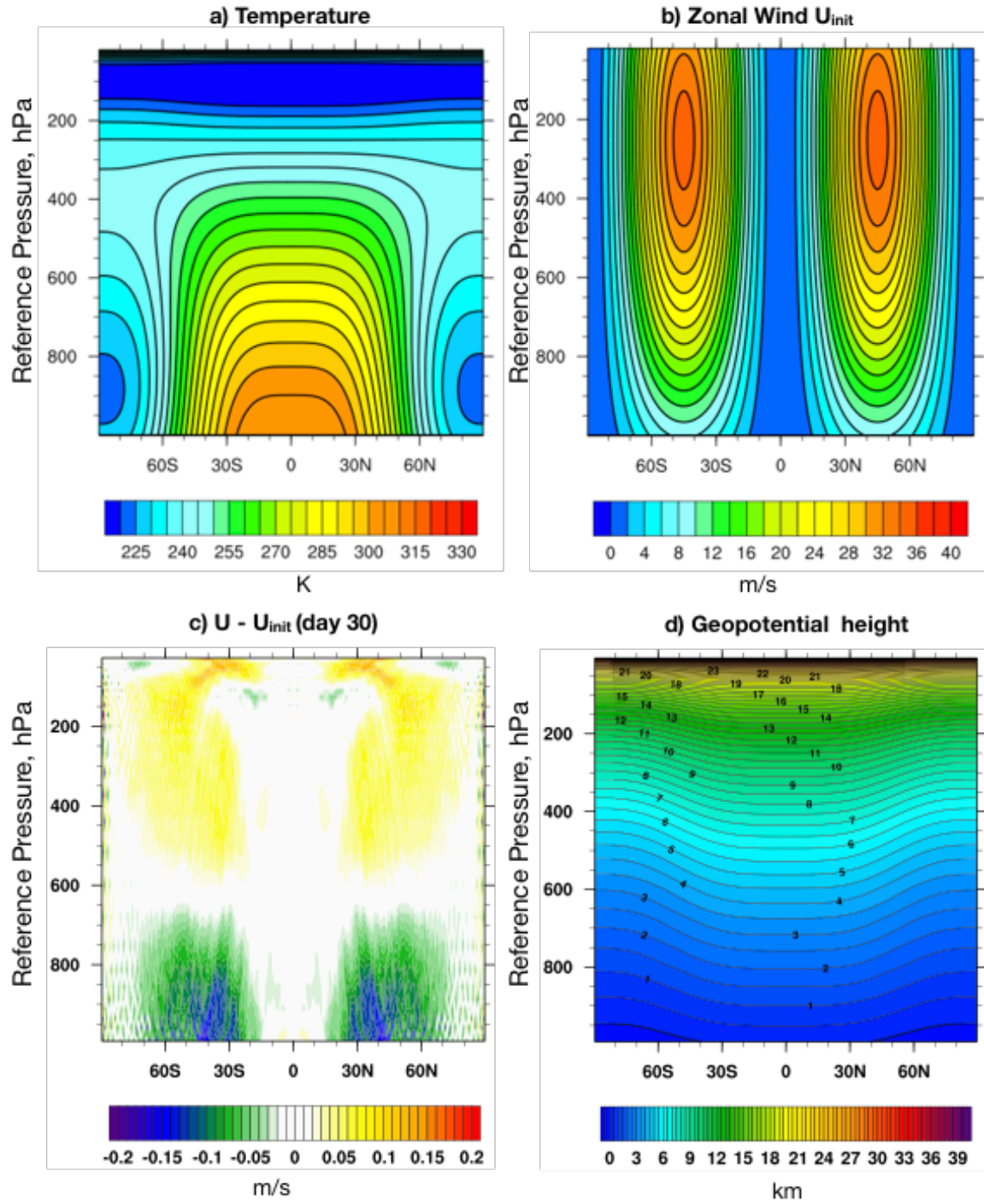


**Figure 1.** Comparison of surface pressure computed by gSAM (top) and ERA5 reanalysis (middle), along with their difference (bottom) after one-hour simulation starting at 00Z on January 2020.

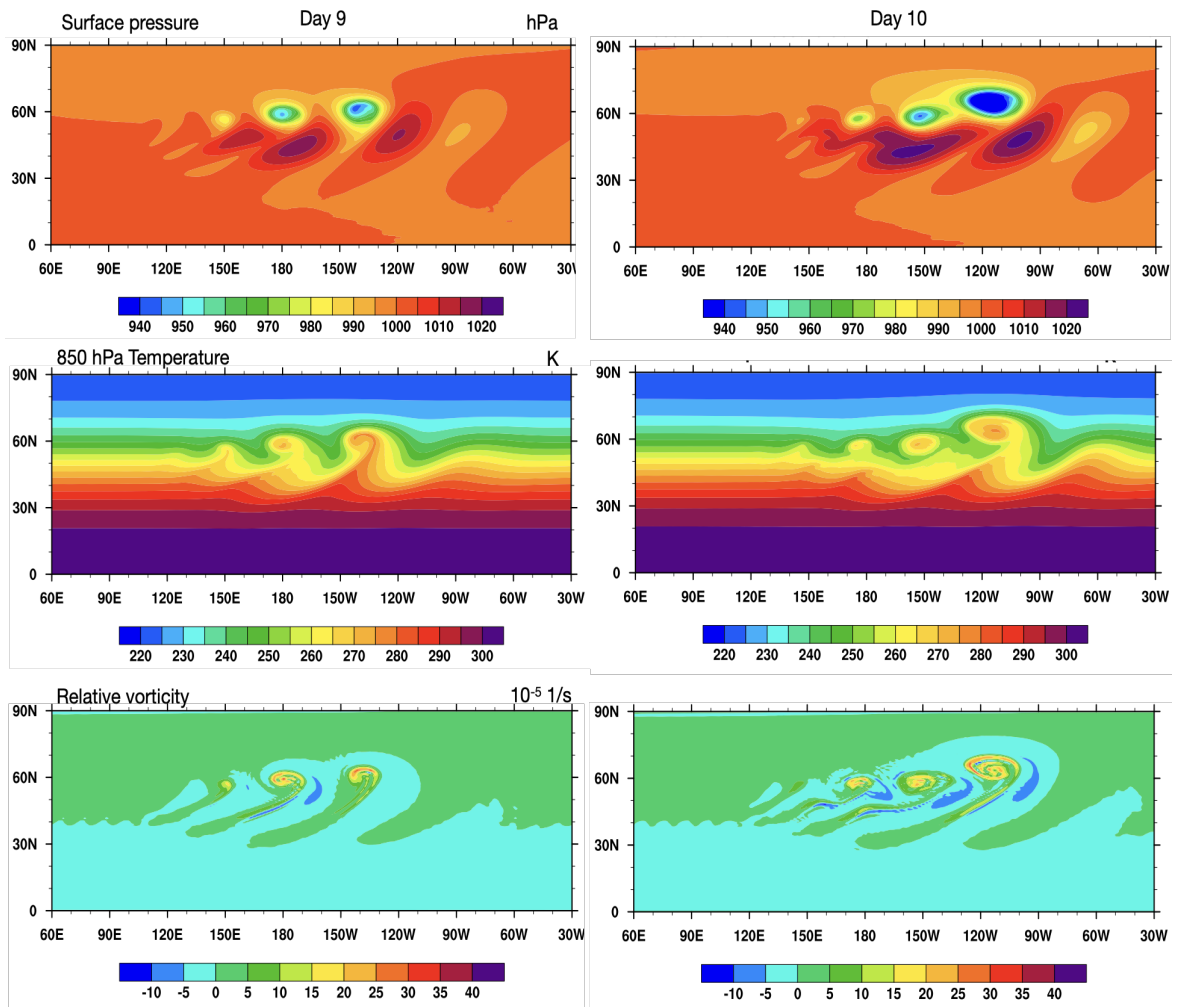
823  
824  
825  
826



827  
 828 **Figure 2.** Initial a) temperature, b) zonal wind, c) pressure, d) geopotential height (zero level  
 829 is shown by thicker isoline), and deviation from initial e) zonal and f) meridional wind after  
 830 30 days of SAM integration in the steady state test.  
 831

832  
 833

834  
835



836

837 **Figure 3.** (top) Surface pressure, (middle) temperature at 850 hPa, and (bottom) relative vorticity  
838 at 850 hPa at (left) day 9 and (right) day 10 of the evolution of baroclinically unstable wave.  
839

840

841

842

843

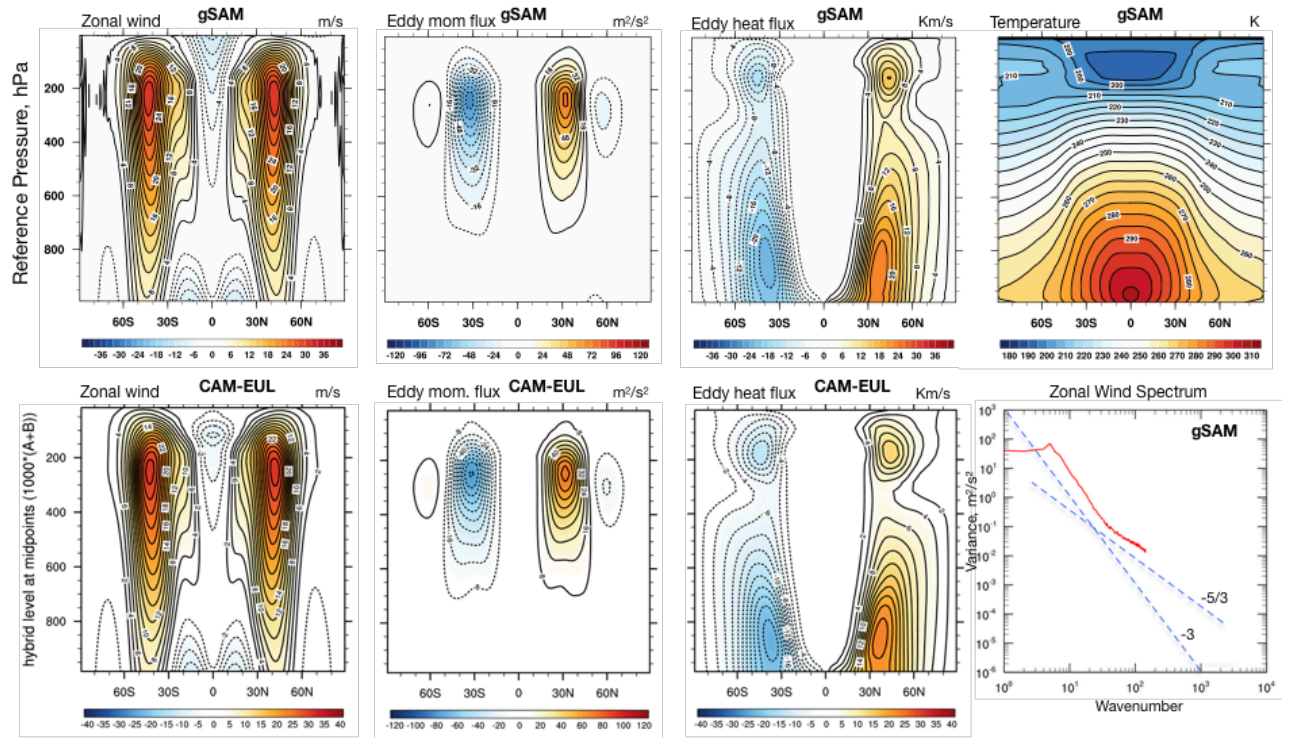
844

845

846

847

848  
849  
850  
851



852  
853  
854  
855  
856  
857  
858  
859  
860

**Figure 4.** 1000-day mean climatology from the Held-Suarez test for various fields for gSAM (top panels) and CAM-EUL (three left bottom panels). The right-bottom panel shows the mid-latitude zonal-wind variance spectrum for gSAM. The panels for CAM-EUL have been adopted from the CESM website <https://www.cesm.ucar.edu/models/simpler-models/held-suarez.html>.

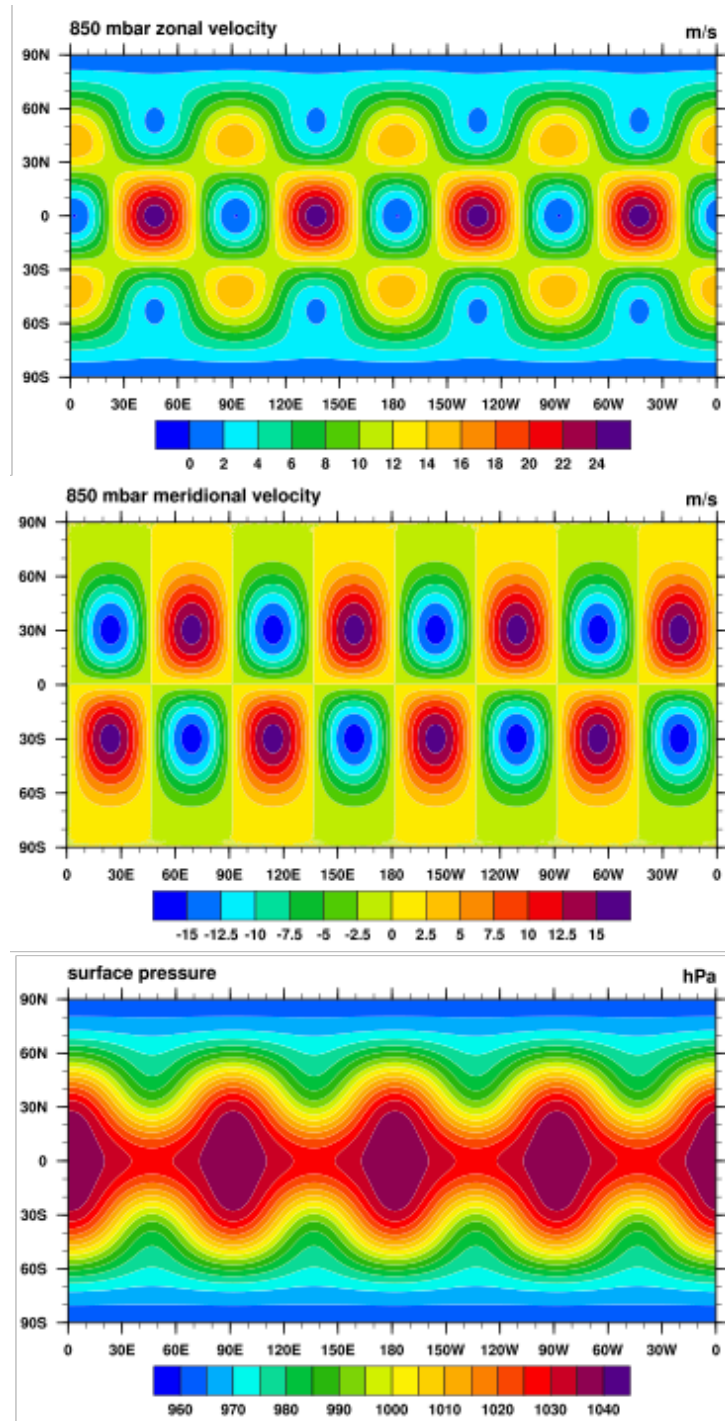


**Figure 5.** The snapshot of the velocity components at 850 hPa levels as well as surface pressure after 24 days of evolution of the Rossby-Haurwitz wave.

861  
 862  
 863  
 864  
 865  
 866  
 867

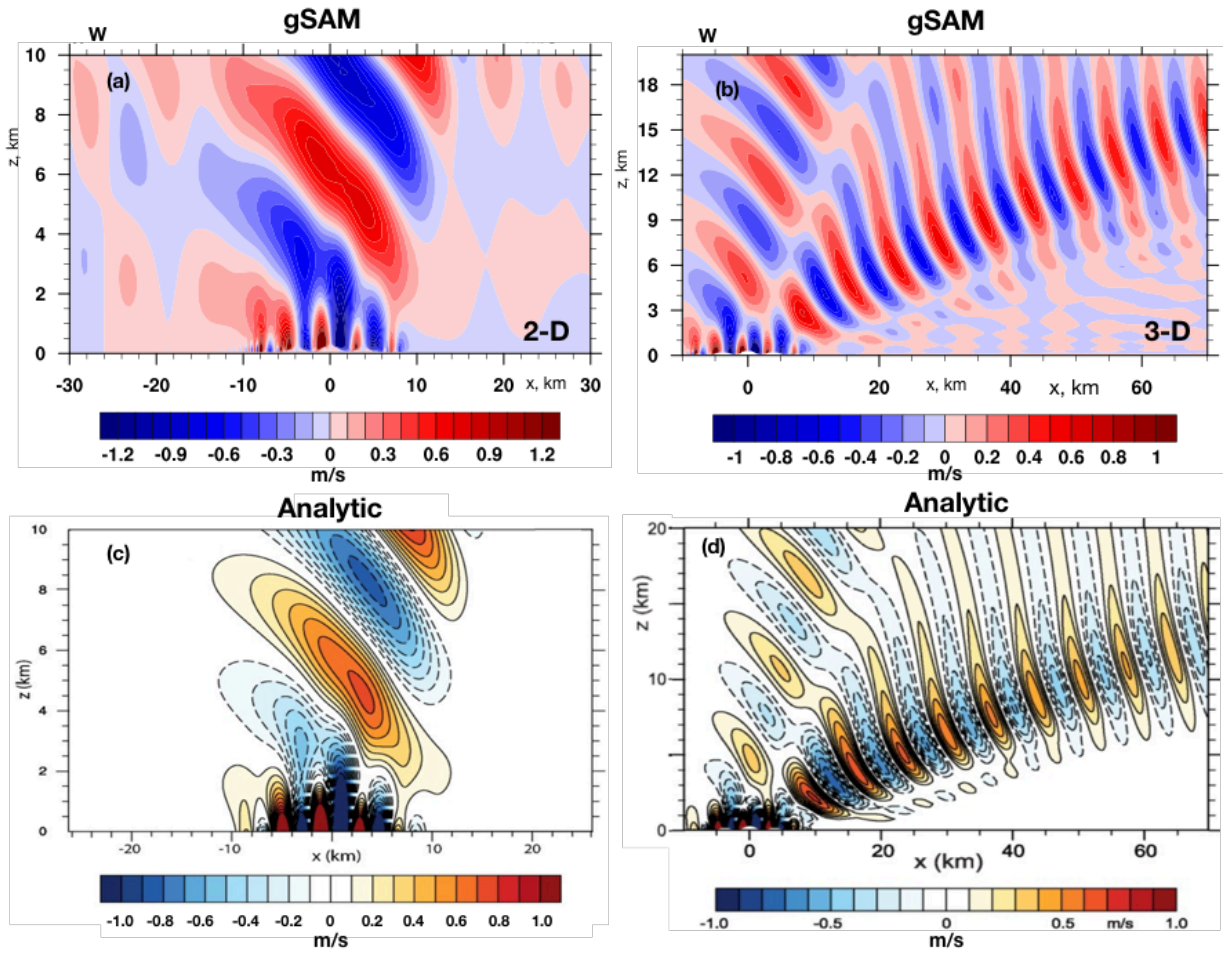
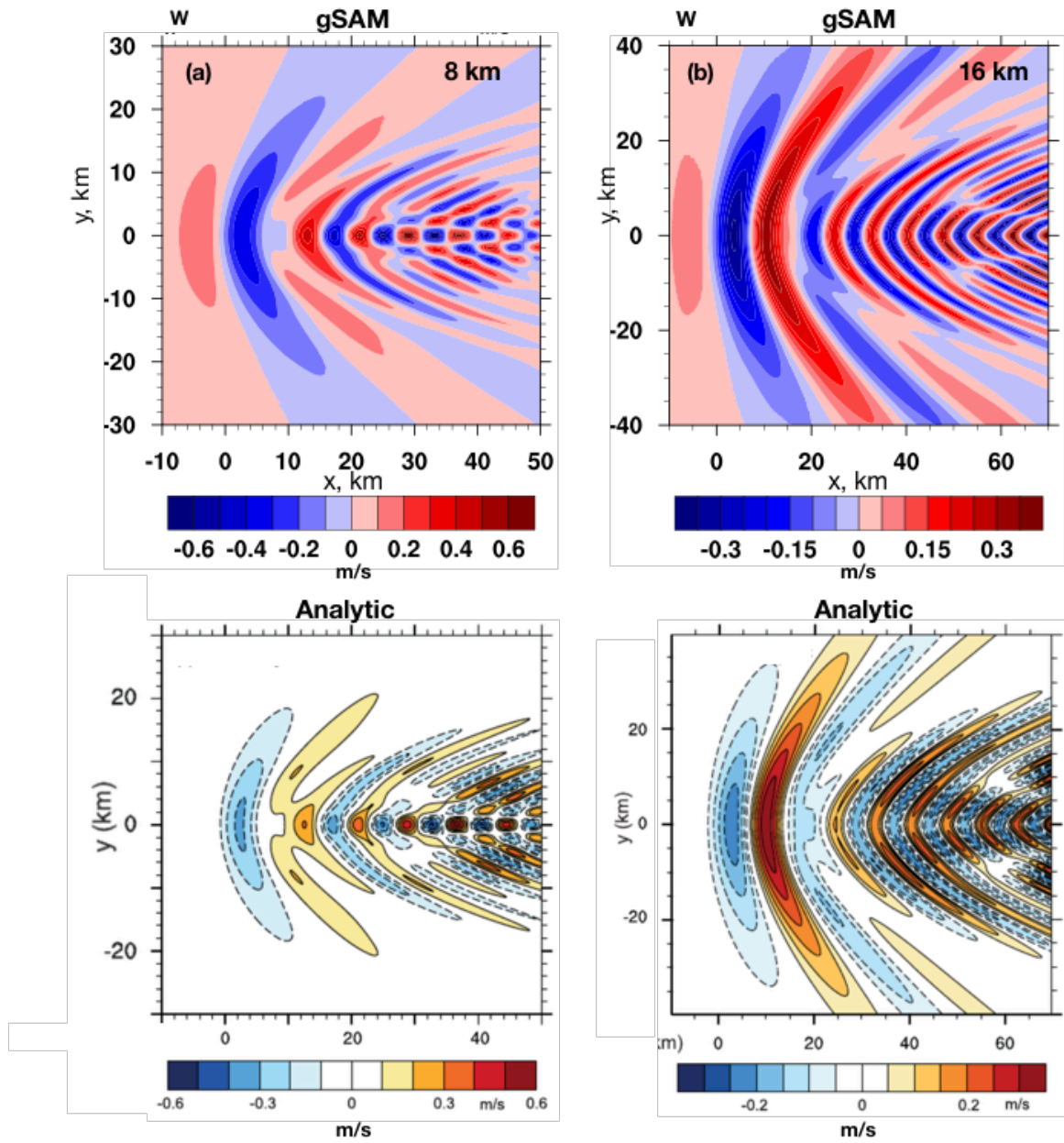


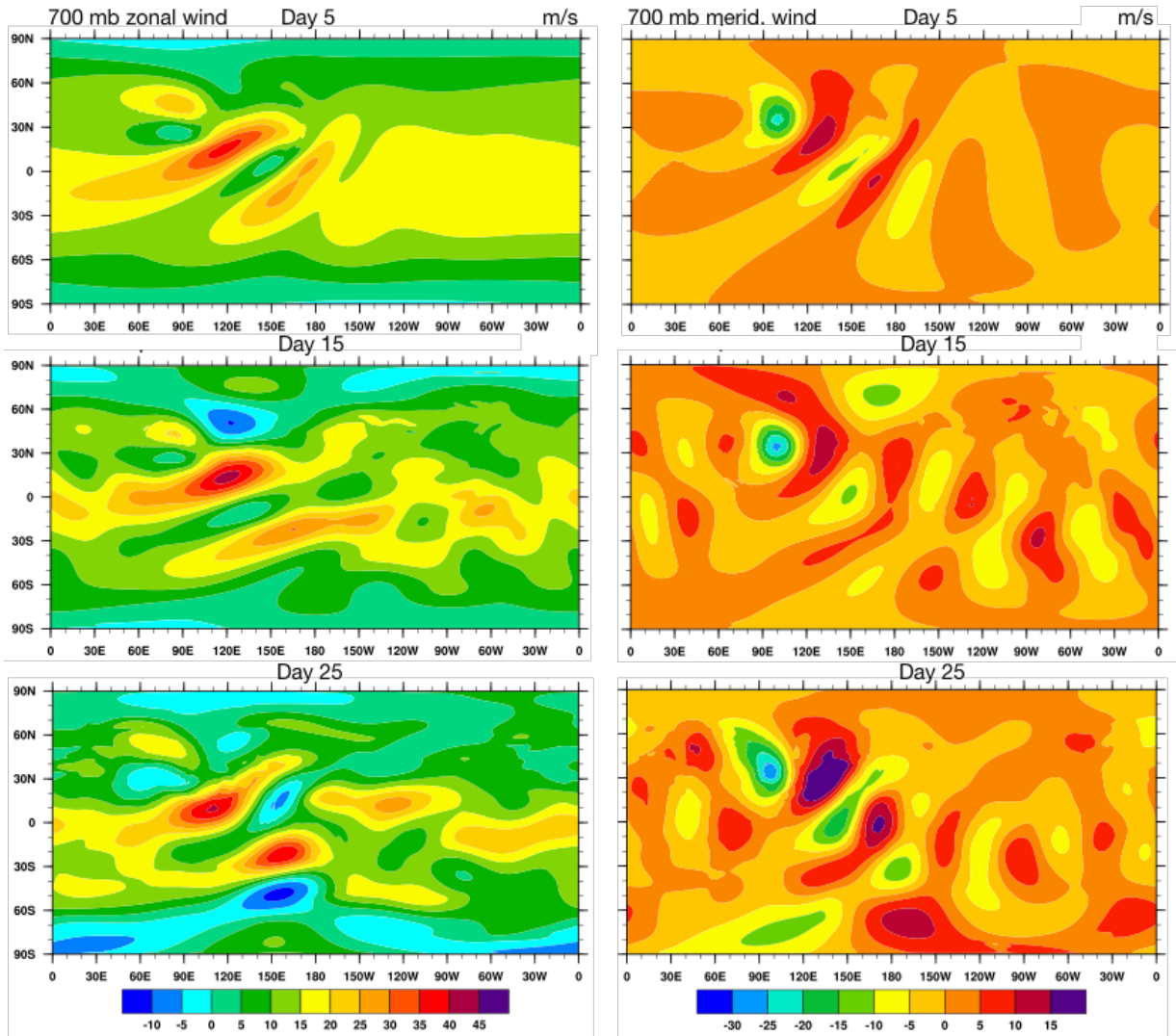
**Figure 6.** Vertical cross section of vertical velocity over a) 2-D and b) 3-D Schär-type mountain ranges. The plots c) and d) for corresponding analytical linear solutions are adopted from Klemp et al (2015).

869  
870  
871  
872  
873  
874  
875  
876  
877  
878  
879  
880  
881



882  
 883  
 884  
 885  
 886  
 887  
 888  
 889  
 890

**Figure 7.** Horizontal cross section of vertical velocity over 3-D Schär-type mountain ranges at c) 8 km and d) 16 km height. The plots c) and d) for corresponding analytical linear solutions are adopted from Klemp et al (2015).



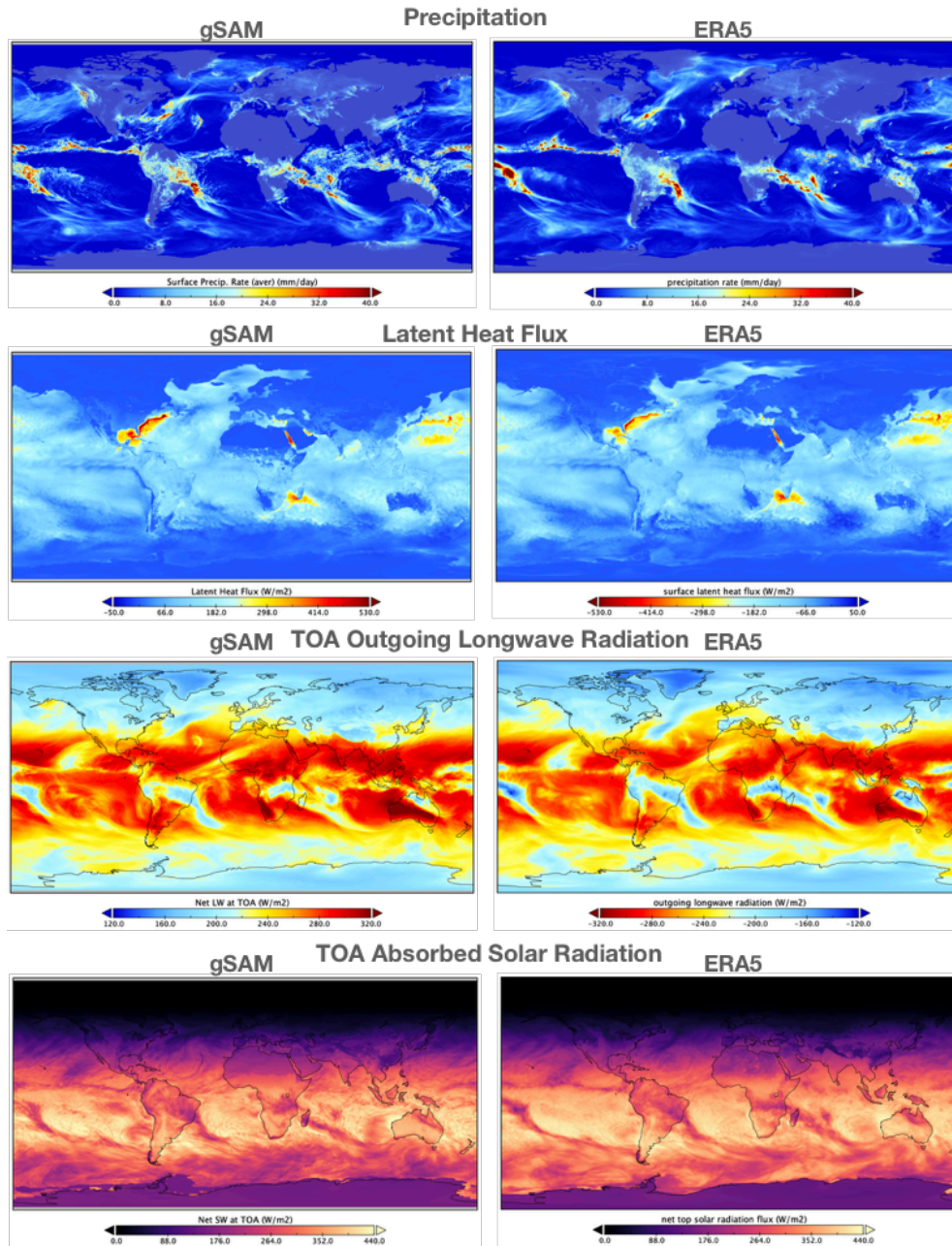
892

893

894

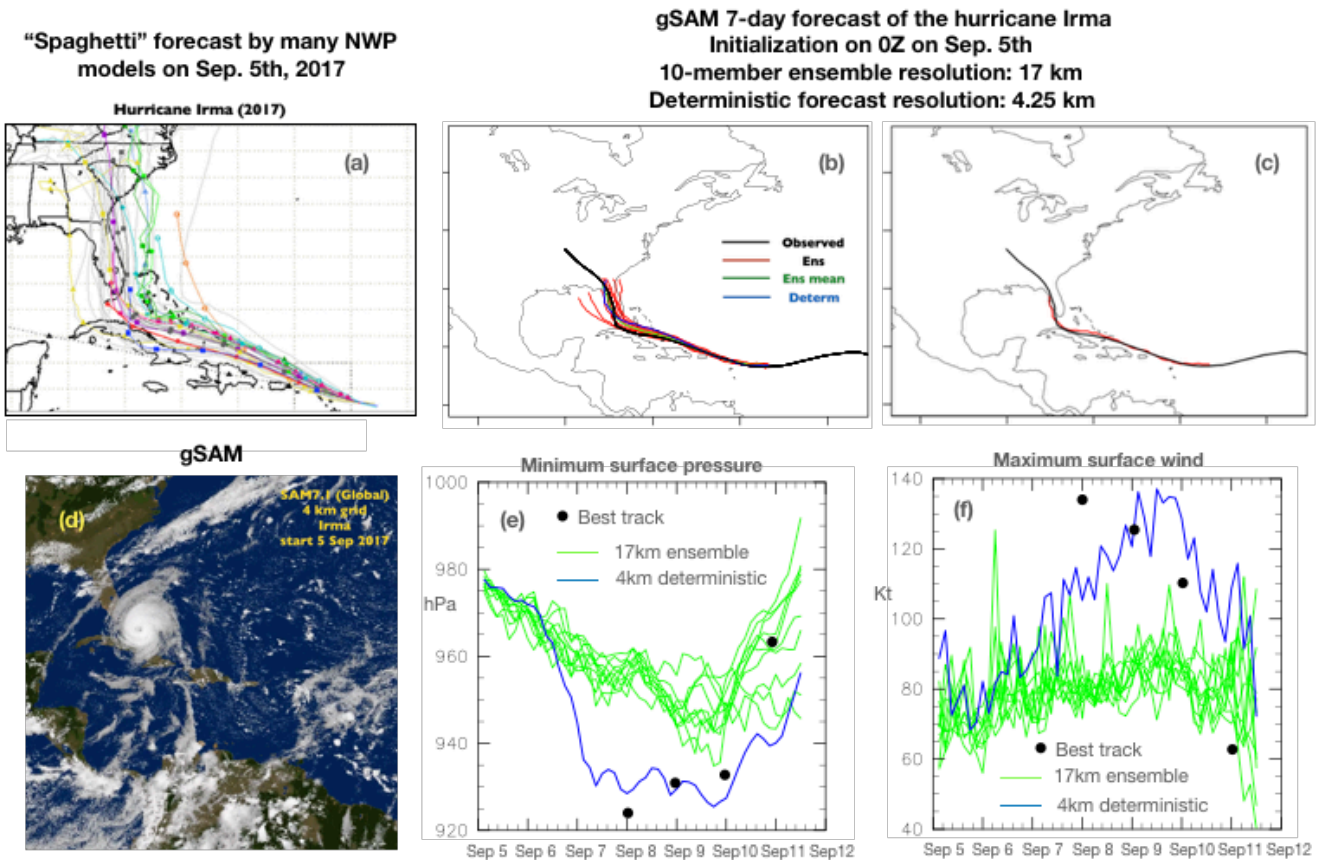
895

**Figure 8.** The snapshots of wind components at 700 mb at (top) day 5, (middle) day 15, and (bottom) day 25 of the Rossby wave-train induced by a circular mountain. The center of the 2-km high and 1500-km wide bell-shaped mountain is at 90°E and 30°N.



896  
897  
898  
899  
900

**Figure 9.** The 5-day (00Z Jan 21 – 00Z Jan 26, 2020) average precipitation rate, latent heat flux, TOA outgoing longwave and absorbed solar radiative fluxes for gSAM (left panels) and ERA4 (right panels).



901  
 902  
 903  
 904  
 905  
 906  
 907  
 908  
 909

**Figure 10.** (a) "Spaghetti" forecast from NWP models as of September 5; (b) tracks predicted by gSAM: 10-member ensemble (red) and ensemble mean (green), deterministic (blue), and best-track (black); (c) track of one of the "lucky" ensemble members; (d) simulated satellite view of Irma using predicted fields from gSAM; (e) minimum surface pressure and (f) maximum surface wind for ensemble members (green) and deterministic run (blue). Best-track data are denoted by black dots.